Weathering Trends Unveil K-Metasomatism in Bundelkhand Granitoids: Resolving the Pink–Grey Granitoid Paradox

Shiba Shankar Acharya[#], Arnab Sain[#], Pragnyasini Behera, Adri Basak, Gautam Kumar Deb

Department of Geology, Presidency University, Kolkata, West Bengal-700073

Corresponding Authors

S.S. Acharya: shiba.geology@gmail.com

A. Sain: arnab.geol@presiuniv.ac.in

Abstract

The petrogenetic puzzle of pink coloration of granitoid rocks is rooted on the debate between primary magmatic versus metasomatic origin of K-feldspar, which, in turn, has persisted due to difficulties in distinguishing these processes through conventional petrographic methods. This study introduces a novel approach using chemical weathering patterns in ACNK ternary diagrams (Al_2O_3, CaO + Na_2O, and K_2O) to identify K-metasomatic signatures in the Bundelkhand granitoids. The method exploits the fact that normal weathering results predictable trends sub-parallel to the A-CN axis, while K-metasomatism creates distinctive deviations toward the K-apex. Three weathered granite profiles spanning pink and grey granitoid varieties were analysed using integrated bulk geochemistry and SEM-EDS microanalysis. Chemical weathering trajectories revealed diagnostic K-metasomatic signatures in pink granitoids, confirming their secondary origin from grey protoliths. This finding reconciles the puzzling identical radiogenic ages of both the colour varieties of granitoids, reported in previous studies.

Petrography of fresh samples suggests biotite chloritization as the fundamental alteration mechanism, operating under shallow crustal conditions (200-350°C), deduced through chlorite thermometry and mineral assemblages. This process drove cascading reactions including albitization, sericitization, epidote formation, and ultimately hematite precipitation responsible for pink coloration of the granitoids. Micropore networks within altered plagioclase served as conduits for fluid migration, enabling pervasive K-feldspathization without requiring major structural controls.

The integrated methodology reveals link between surface weathering and deep crustal metasomatism, providing the surface process as a powerful diagnostic tool for identifying cryptic alteration in granitoids. These findings have significant implications for understanding Archean crustal evolution and the petrogenetic interpretation of ancient granitoid terranes.

Keywords: K-metasomatism, ACNK ternary diagram, Bundelkhand granitoids, Biotite chloritization, Plagioclase micropore networks

1. Introduction

The persistent coexistence of pink and grey granitoids within the same plutonic complex of the Bundelkhand Craton(Ray et al. 2016; Sensarma et al. 2018; Bhattacharjee and Ahmad 2023) presents a fundamental petrogenetic puzzle that reflects broader global debates on the mechanism of granite coloration (Putnis et al. 2007; Plumper and Putnis 2009; Morad et al. 2010). The characteristic pink (or red) coloration of many granitic rocks has long been attributed to the presence of ferric iron oxides, probably hematite (Fe_2O_3), in the alkali feldspar which form a major constituent of such rocks (Boone 1969; Taylor 1977; Nakano et al. 2005). The hematite is assumed to occur as sub-microscopic inclusions, which have either crystallized together with the feldspar from a granitic melt, or have exsolved out by solid state exsolution from an Fe^{3+}-bearing solid solution $[(K,Na)(Al,Fe^{3+})Si_3O_8]$, or, as a third possibility, have been introduced by Fe-bearing fluids subsequent to crystallization of the granite body (Putnis et al. 2007).

The stakes in this argument are particularly high for the Bundelkhand granitoids, as this craton represents one of the rare fragments among the less than 10% of Archean continental crust preserved today. Moreover, pink granitoids dominate this ~29,000 km^2Archean nucleus, with punctuated only by a few coexisting patches of grey granitoids (Ray et al. 2016; Kaur et al. 2016; Sensarma et al. 2018; Bhattacharjee and Ahmad 2023; Rout et al. 2025). The craton is further distinguished by NE–SW oriented, equally spaced Giant Quartz Veins (Pati et al. 2007). A comparable Archean setting is found at Malanjkhand, India, where copper mineralization occurs within fracture-controlled quartz reefs hosted by pink granitoid bodies and surrounded by grey granitoids (Panigrahi and Mookherjee 1997).

Two competing hypotheses have emerged to explain the grey *vs.* pink/red colour dichotomy in Bundelkhand granitoids. Primary magmatic hypotheses invoke separate emplacement events, with some researchers proposing two discrete magmatic pulses around 2.5 Ga (e.g., Ray et al. 2016), while others suggest cogenetic emplacement with inherent compositional variations (Bhattacharjee and Ahmad 2023). Although these studies identified that the pink granitoids are rich in K-feldspar, they considered them as primary and do not comment about the presence or absence of hematite, if any. In contrast, metasomatic hypotheses attribute the pink coloration (described as red granitoids) to post-emplacement fluid alteration. However, in case of Bundelkhand granitoid, Sensarma et al. (2018) proposed that high-temperature replacement of microcline and oligoclase in grey granitoids resulted in the formation of albite, followed by growth of K-feldspar (microcline) at the expense of altered plagioclase formed earlier. They hypothesized that high-temperature Fe–Mg–Na–K-rich fluids (~950°C) of crust-mantle derivation re-equilibrated original grey monzogranite, potentially linked to Paleoproterozoic mafic dyke intrusions. However, recently, Rout et al. (2025) suggested that the fluid responsible for alteration is of lower-temperature and unrelated to dyke emplacement, marked by variable degrees of sericitization of plagioclase and the chloritization of hornblende and biotite.

The major difference between these two diverging opinions boils down to the mode of formation of K-feldspar i.e. whether the pink varieties host primary magmatic or secondary K-feldspar or have a metasomatic origin, or even both. Metasomatic processes may not be easily recognized unless they are associated with the formation of new minerals characteristic of fluid infiltration (e.g., related to ore body emplacement), or unless successive stages in the replacement can be identified, as in the San Marcos granites (Putnis et al. 2007). However, it is very unlikely that a fluid-induced K-metasomatism can affect the entire granitoid outcrop in the similar way (Algeo et al. 2025). Therefore, deviation from an ideal weathering trend can be used as a diagnostic tool to solve the above primary vs metasomatic effect. Recently, Algeo et al. (2025) have reviewed the use of the spread of chemically weathered samples in ACNK ternary diagrams (i.e., with apices of Al_2O_3, CaO + Na_2O, and K_2O) to decipher the K-metasomatism. Normal weathering produces predictable linear trends sub-parallel to the A-CN axis, while K-metasomatism disrupts these patterns by introducing K-enrichment that creates diagnostic deviations toward the K-apex (Fedo et al. 1995; Algeo et al. 2025).

With an integrated approach of petrography and SEM-EDS microanalysis of fresh samples together with bulk geochemical analysis of three weathered granite profiles, the present study employs chemical weathering behaviour as a diagnostic tool to first confirm the presence of K-metasomatic signatures in Bundelkhand granitoids, then to elucidate the mechanisms responsible for this K-enrichment. It is further demonstrated how felsic fluids exploited micropores within plagioclase as conduits for K-feldspathization, with subsequent hematite formation producing the characteristic pink colour, resolving thus a fundamental question concerning Archean crustal evolution in the Bundelkhand Craton.

2. Geological Setup

The Bundelkhand Craton, occupying a semicircular area of approximately 29,000 km² in north-central Peninsular India (24.5°–25.5° N, 78°–80.5° E), represents one of the most significant Archean nuclei in the northern Indian Shield(Pati 2020). This cratonic block is bounded by Paleoproterozoic rocks of the Vindhyan Supergroup to the east, west, southeast, and southwest, with Deccan Trap volcanics occurring further southwest, while its northern exposure is delimited by Indo-Gangetic alluvium (Fig. 1) (Mondal et al., 2002; Pandey et al., 2011).

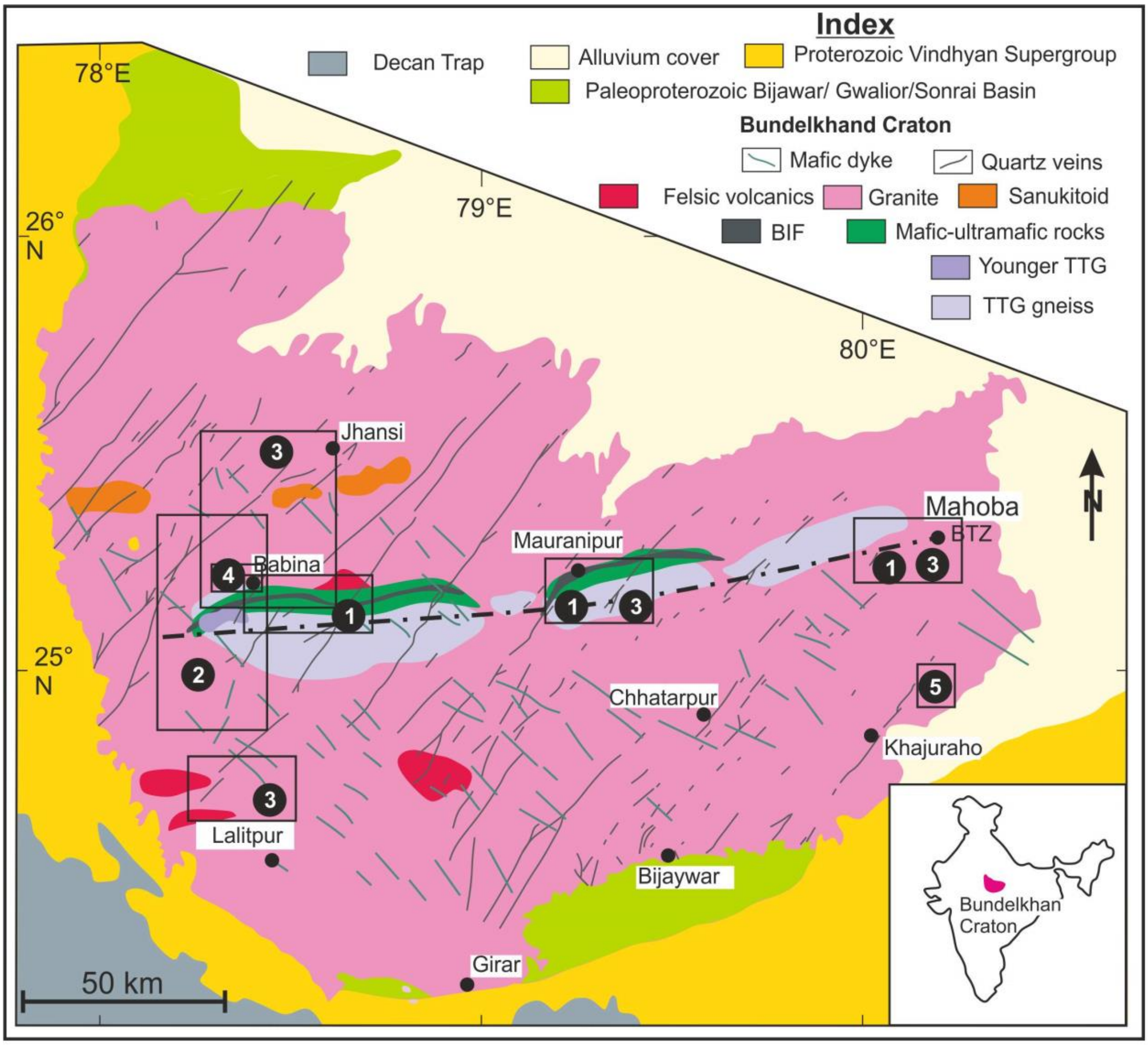

Fig. 1 Geological map of the Bundelkhand craton compiled from Basu (1986), Mondal et al. (2002), Singh et al. (2021), and Slabunov and Singh (2021b). Inset shows the location of the Bundelkhand craton within the Indian subcontinent. Numbered boxes indicate study areas of

previous investigations: (1) Kumar et al. (2021); (2) Bhattacharjee and Ahmad (2023); (3) Kaur et al. (2016); (4) Singh et al. (2021); (5) Sanyal et al. (2025).

The craton is primarily composed of ~ 3.5 to ~ 2.6 Ga Tonalite–Trondhjemite–Granodiorite (TTG) gneisses (Joshi et al. 2017, 2022; Singh et al. 2021; Malviya et al. 2022) ~ 3.4 to ~ 2.5 Ga Bundelkhand greenstone complexes including the Babina-Mauranipur-Mahoba belt and the Girar belt in the central and southern parts respectively (Malviya et al. 2006; Singh and Slabunov 2016); 2.58 to 2.49 Ga Bundelkhand granitoids littered with mafic enclaves (Basu 1986; Ray et al. 2016; Kaur et al. 2016; Kumar et al. 2021); ~1.8 to 1.63 Ga Giant Quartz Veins (Slabunov and Singh 2022) and dolerite dyke swarm emplaced during three distinct episodes at 1.98 Ga, 1.8 Ga and ~1.0 Ga (Pradhan et al. 2012; Shankar et al. 2023). Among all these litho-types the Bundelkhand granitoids represent the most dominant one which includes syeno-to monzo-granite, granodiorite and diorite, and occupies >90% of the craton (Mondal et al. 2002; Kaur et al. 2016).

Although detail structural and metamorphic evolution is not available, sporadic deformation features have been considered as records of polyphase deformation history of the Bundelkhand craton (e.g., Deb and Bhattacharyya 2022). The Bundelkhand craton also witnessed at least three phases of metamorphism(Sibelev et al. 2021a). The 1stphaseMesoarchean (ca 2.8 Ga) eclogite facies metamorphism have been reported from the Central Bundelkhand Greenstone Belt (Saha et al. 2011) whereas the 2nd phase Neoarchean (ca. 2.7 Ga) amphibolite metamorphism is more widespread. The latest metamorphic event took place at Paleoproterozoic time (ca 1.9–1.8 Ga), under prehnite-pumpellyite-facies and the event is locally associated with GQV formation.

The Bundelkhand granitoids (occupying >90% of the exposed area), varying in color, texture, mineralogy, and geochemistry, were possibly emplaced in an arc-related setting (Jhingran 1958; Basu 1986; Mondal et al. 2002; Kaur et al. 2016; Joshi et al. 2017; Singh et al. 2021). The two main color variants, grey and pink to red granitoids, show wide variation in outcrop distribution. Previous studies suggest that pink granitoids are more abundant across the craton (Kaur et al. 2016; Sensarma et al. 2018; Bhattacharjee and Ahmad 2023). But other observations indicate a higher proportion of pink granitoids, particularly in the southern part of the craton (Ray et al. 2016).The question of whether colour variations in Bundelkhand granitoids result from separate emplacement events, cogenetic batches with inherent compositional differences, or secondary metasomatic alteration by hydrothermal fluids remains actively debated. Evidence for extensive fluid-rock interaction includes: (1)

pervasive K-metasomatism and albitization processes documented in feldspar replacement reactions (Sensarma et al. 2018); (2) high-temperature (≥950°C) Fe-Mg-Na-K-rich fluid infiltration linked to mafic dyke swarm activity causing reddening of granitoids through precipitation of Fe-rich particles in porous feldspars (Sensarma et al. 2018); (3) hydrothermal alteration associated with Cu-Au mineralization involving potassic, chloritic, and iron alteration in ore zones (Rana et al. 2023); and (4) fluid-assisted rejuvenation of brittle fractures leading to ductile shear zone development with at least five growth stages documented in the granitoid rocks (Sarkar et al. 2020). These processes collectively indicate that post-magmatic hydrothermal alteration has significantly modified primary magmatic signatures, complicating the interpretation of original compositional variations (Ray et al. 2016; Kaur et al. 2016). However, the nature and source of the metasomatic fluid as well as mechanism of alteration, leading to pink coloration of the original grey granitoids, are yet to be established. In this regard samples from the profiles that record least altered to completely weathered varieties beneath soil cover have never been tested from this craton.

3. Methodology

3.1 Field Sampling

During two consecutive field seasons, three weathering profiles (L1–L3; Fig. 1) were studied near Khajuraho in the southeastern Bundelkhand Craton. These profiles represent pink, grey, and mixed granitoid varieties, respectively. At each profile, multiple samples were systematically collected from distinct weathering horizons, yielding a total of twenty-four specimens. All sampling followed established in situ weathering protocols to preserve primary petrographic textures and geochemical gradients. Additionally, fresh outcrop specimens of pink and grey granitoids were gathered from multiple exposures in the Chhatarpur, Bijawar, and Khajuraho areas for comparative petrographic and geochemical characterization.

3.2 Geochemical Analysis

All weathered rock samples were powdered to <75 µm using an agate mortar and pestle to minimize contamination. Major-element abundances were determined by wavelength-dispersive X-ray fluorescence (PANalytical AXIOS) at Presidency University, Kolkata, using the SUPERQ matrix-correction algorithm and eight international rock standards. Analytical accuracy and precision were assessed using Geological Survey of Japan standards JG-1 (granodiorite) and JG-2 (granite), achieving accuracy and precision better than 5%.Fourteen samples from the L1 and L2 profiles, representing pink and grey granitoids respectively, were selected for trace-element analysis including rare earth elements (REEs). These samples underwent two-stage acid digestion (HF–HNO_3 followed by HNO_3–HCl) in a Class 100 clean room facility at the Indian Institute of Science, Bangalore. Trace elemental concentrations were determined by inductively coupled plasma–mass spectrometry (Thermo iCAP-RQ), with external reproducibility of better than 5% (REEs < 2%). Calibration was performed using USGS reference materials BHVO-2 and BCR-2, while analytical accuracy was verified through analysis of the USGS.

3.3 Petrographic and Microanalytical Studies

Multiple thin sections (n=12) of fresh samples from each granitoid variety were examined under plane- and cross-polarized light using a Nikon Eclipse LV100POL polarizing microscope to document mineral textures and alteration rims. Morphological and textural characterization of samples, along with chemical analyses of mineral phases, were performed using scanning electron microscopy coupled with energy dispersive X-ray spectrometry (SEM-EDS). The analyses were conducted using a JEOL JSM-IT500 scanning electron microscope at Presidency University, equipped with energy dispersive spectrometry capabilities. Observations were made on the same thin sections used for petrographic characterization. Prior to SEM analysis, the slides were gold-coated using a DII-29030SCTR Smart Coater to ensure optimal conductivity and minimize charging effects. Backscattered electron detector compositional (BED-C) imaging was employed to reveal compositional contrasts and document microtextural relationships between mineral phases and host lithologies at the microscale. Energy dispersive spectrometry (EDS) analyses of individual mineral phases provided semi-quantitative elemental compositions of both primary (e.g., plagioclase) and secondary phases (e.g., titanite, chlorite). The analysis of the chlorite data from EDS were performed through the WinCcac program (Yavuz et al. 2015).

3.4 Calculated Indices and mineral formulae

The degree of weathering of the studied samples was quantified using the Chemical Index of Alteration (CIA) following Nesbitt and Young (1982), calculated from molecular proportions according to:

$$CIA = [Al_2O_3/(Al_2O_3 + CaO^* + Na_2O + K_2O)] \times 100$$

Where CaO^* represents calcium oxide in the silicate fraction after correction for non-silicate sources. The CaO^* correction followed McLennan (1993), wherein if the molar content of CaO (after phosphate correction using P_2O_5) is less than that of Na_2O, this CaO value was adopted as CaO^*. If the molar CaO content exceeds Na_2O, CaO^* was assumed equivalent to Na_2O.

Individual mineral formulas were determined from semi-quantitative EDS analysis of selected grains. Atomic proportions of constituent elements were calculated from normalized atomic percentages obtained through standardized EDS protocols and compared to stoichiometric mineral compositions. Mineral phases were identified based on best-fit comparisons between observed and theoretical atomic ratios, with structural formulas calculated using appropriate crystallographic normalization schemes.

4. Results

4.1 Outcrop pattern

Three weathering profiles (K-L1 to K-L3; Fig. 2a) were sampled around Khajuraho (K-L1: 24°50′39.4″ N, 79°57′59.1″ E; K-L2: 24°51′9.5″ N, 79°57′21.3″ E; K-L3: 24°52′26.8″ N, 79°58′54.2″ E). Each profile, 2–4 m high, begins with a 10–20 cm soil horizon. Depending upon the colour of the relict least weathered granitoid and surrounding outcrops, the above three profiles exhibit distinct varieties of granitoids, samples of K-L1 represents pink granitoid, K-L2 grey, and of K-L3 display a mixed, intermediate colour. Quartz- and pegmatite-veins (5–50 cm thick) crosscut both weathered zones and, where exposed, the fresh granite.

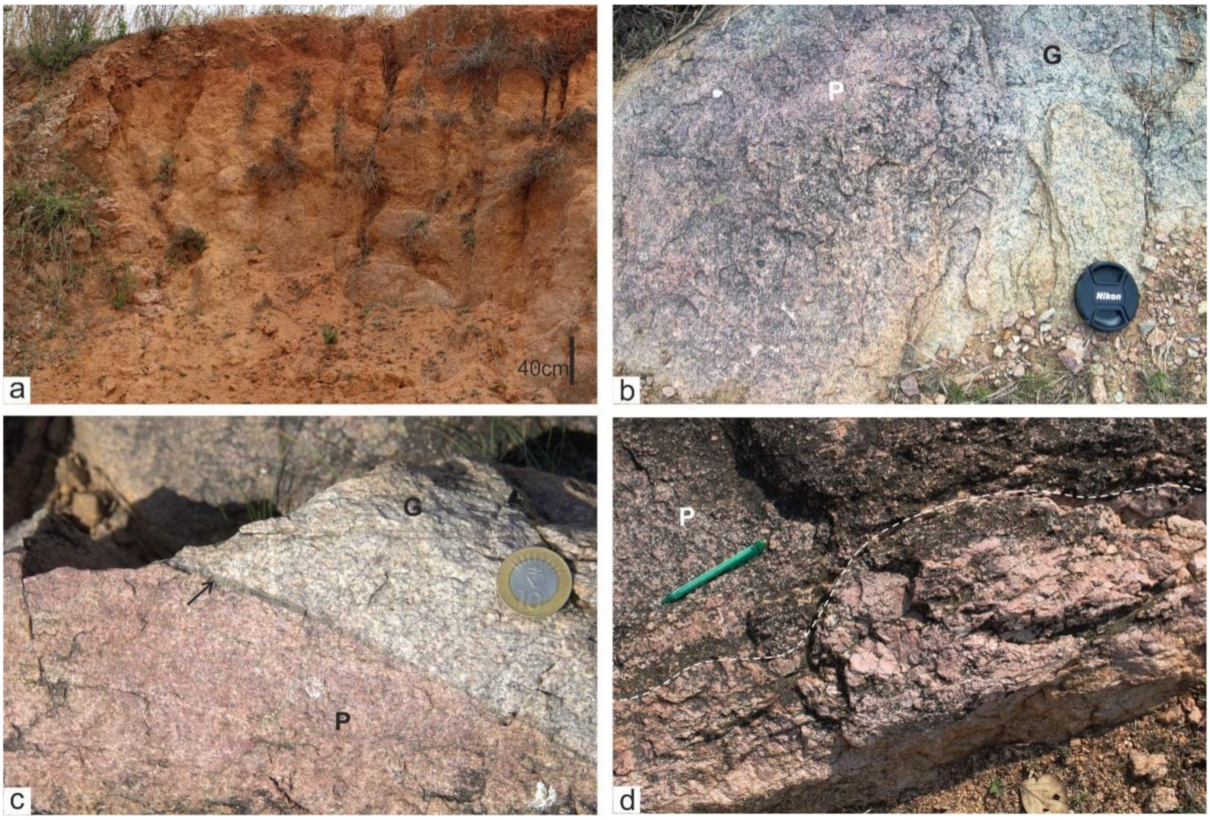

Fig. 2 Outcrop features of the study area. (a) Weathered granite profile from the pink granitoid domain. (b) Gradational contact between pink granitoid (P) and grey granitoid (G). (c) Sharp contact between pink granitoid (P) and grey granitoid (G), with fine-grained epidote-bearing zone along the contact (black arrow). (d) Pink pegmatitic vein intruding the granite (P) host rock.

Outcrops of the granitoid rocks in most locations near Khajuraho, Chattarpur and Bijawar regions of Madhya Pradesh show that the pink and grey varieties occur side by side, with gradational contacts, marked by the millimetre- to centimetre-scale transition zones (Fig. 2b). However, near Khajuraho, sharp contacts are separated by 1–4 mm fine-grained, epidote-bearing veins (Fig. 2c). Locally, pink coloured pegmatite occurs as intrusive veins within grey granitoid (Fig. 2d). Intensity of colour in the pink granite varies from light pink through pink to mauve. Both the pink and grey granites are usually medium- to coarse-grained, and with or without relict phenocrysts of feldspar.

4.2 Geochemical characteristics

The bulk geochemical compositions of the studied samples are presented in Table S1 (Supplementary file 1). The results of the EDS analysis used for formulating the alteration reactions through stoichiometric mineral formulas are given in Supplementary Tables S2 and

S3 (given within Supplementary file 1). The average SiO_2 concentration of the pink granitoids (K-L1) is generally higher than those of the grey granitoids (K-L2). A strong negative correlation between Al_2O_3 and SiO_2 ($r = -0.86$, $p < 0.001$) is observed across all studied samples. Among all weathered samples of pink granitoids, K_2O exhibits a strong negative correlation with Na_2O ($r = -0.92$, $p < 0.001$) and CaO ($r = -0.67$, $p < 0.001$), unlike the other two profiles (Figs. 3a-3b).

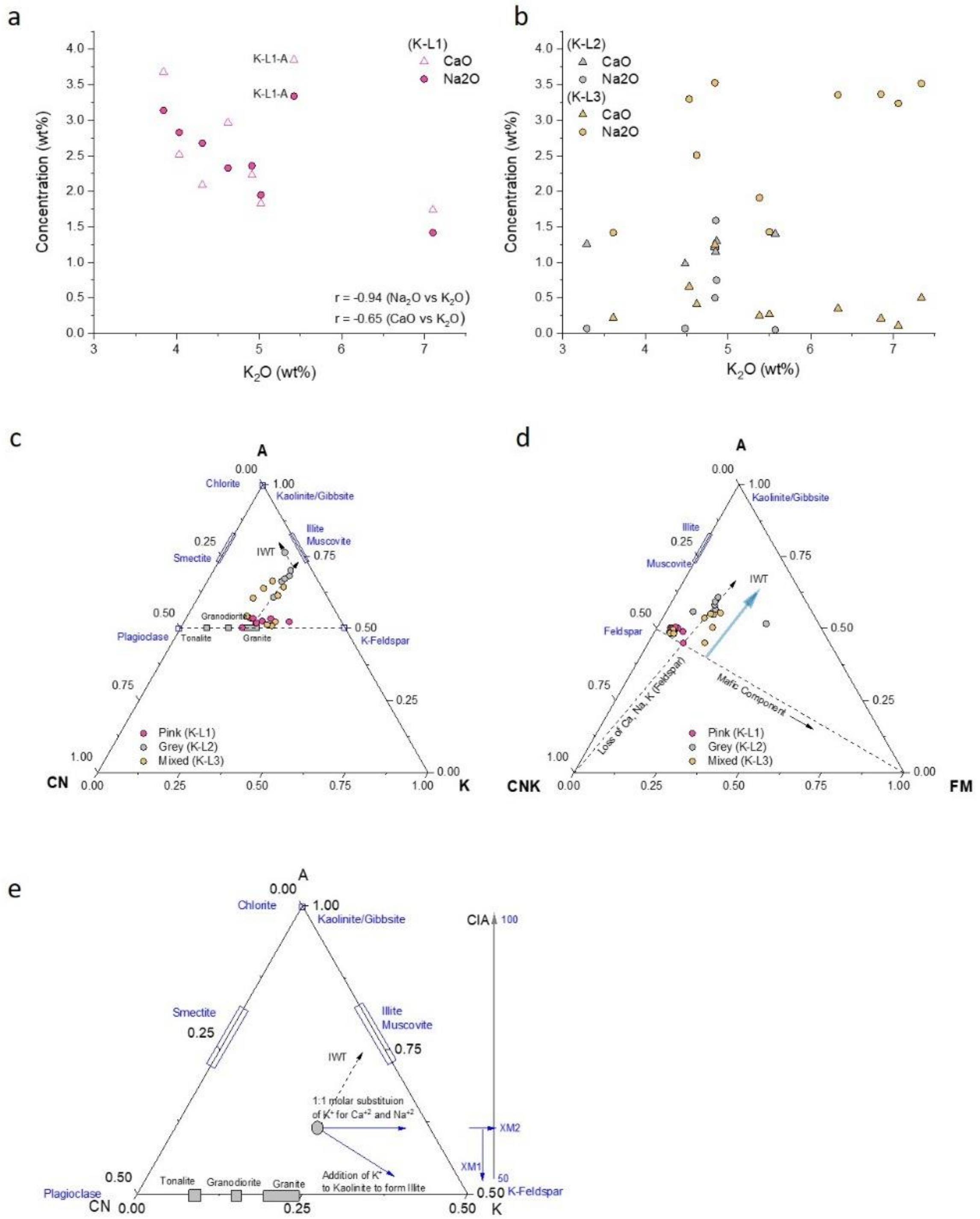

Fig. 3 Compositional differences between pink and grey granitoid weathered samples. (a) Both CaO and Na_2O show negative correlation with K_2O in the pink granitoid weathered profile (K-L1), whereas (b) this relationship is absent in the grey (K-L2) and mixed (K-L3) profiles. The surface sample (K-L1-A) was excluded in the correlation calculations. (c) The A-CN-K ternary plot reveals normal weathering trends in grey granitoids, in contrast to K-metasomatism effects in pink and mixed granitoid samples. (d) The A-CNK-FM plot shows similar weathering trends and elevated mafic content in grey granitoid samples. (e) Different evolutionary paths of weathered samples in the A-CN-K plot with probable reaction mechanisms (after Fedo et al., 1995; Algeo et al., 2025).

The Chemical Index of Alteration (CIA) values indicate variable weathering intensities: K-L1 samples show incipient weathering (52.4 ± 1), while K-L2 (68.2 ± 4.7) and K-L3 (57.7 ± 6) exhibit moderate to intense chemical weathering. The distribution of samples in the A-CN-K ternary diagram (Fig. 3c) reveals that all K-L2 profile samples (grey granitoids) follow the ideal weathering trend (IWT), which is parallel to the A-CN join. Conversely, all K-L1 (pink) samples and some K-L3 (mixed) profile samples deviate from the IWT, plot towards the K-apex. The A-CNK-FM ternary diagram (Fig. 3d) exhibits similar trends to those observed in the A-CN-K plot, where the K-L2 samples show normal depletion of mobile elements and the mafic contents of K-L1 are different than that of the K-L2.

The chondrite (Sun and McDonough 1989)-normalized REE patterns (Fig. 4a) for both pink and grey granitoids display characteristic Light Rare Earth Element (LREE) enrichment and flat Heavy Rare Earth Element (HREE) patterns. The primary differences between these granitoids are a pronounced negative Eu anomaly and higher overall REE concentrations in K-L2 samples compared to K-L1.The primitive mantle-normalized multi-element spider diagram (Fig. 4b) exhibits distinct negative Nb-P-Ti anomalies in both granite types, where the grey granitoids show higher concentrations.

4.3 Petrography

4.3.1 Grey Granite

Grey granite is essentially composed of K-felds +qtz + plag +biot +chl+ ep and as accessory minerals spn±mag ±ap±zr ± aln ± ttn±ser. K-feldspars including orthoclase, microcline, and perthite occur both as porphyroclast and groundmass constituent (Fig. 5a). Quartz grains vary in size and are usually characterized by undulose extinction and sub-grain formation. The sub-hedral grains of plagioclase exhibit both growth and deformation twinning, and may be either unaltered or weakly altered (into ser+ep) (Fig. 5b). Electron dispersive spectroscopy (EDS) analysis of both altered and unaltered grains indicates composition of pure albite (Ab_{100}) (Table S2). Locally myrmekitic intergrowth is also observed. Small titanite grains are typically aligned along the cleavage planes, defined by chlorite. Epidote occurs both as primary magmatic phase, showing euhedral to subhedral outline (Fig. 5b), and secondary alteration product with irregular outlines. The primary epidote grains are medium-grained and generally associated with secondary chlorite grains as well as inclusion in quartz and feldspar grains.

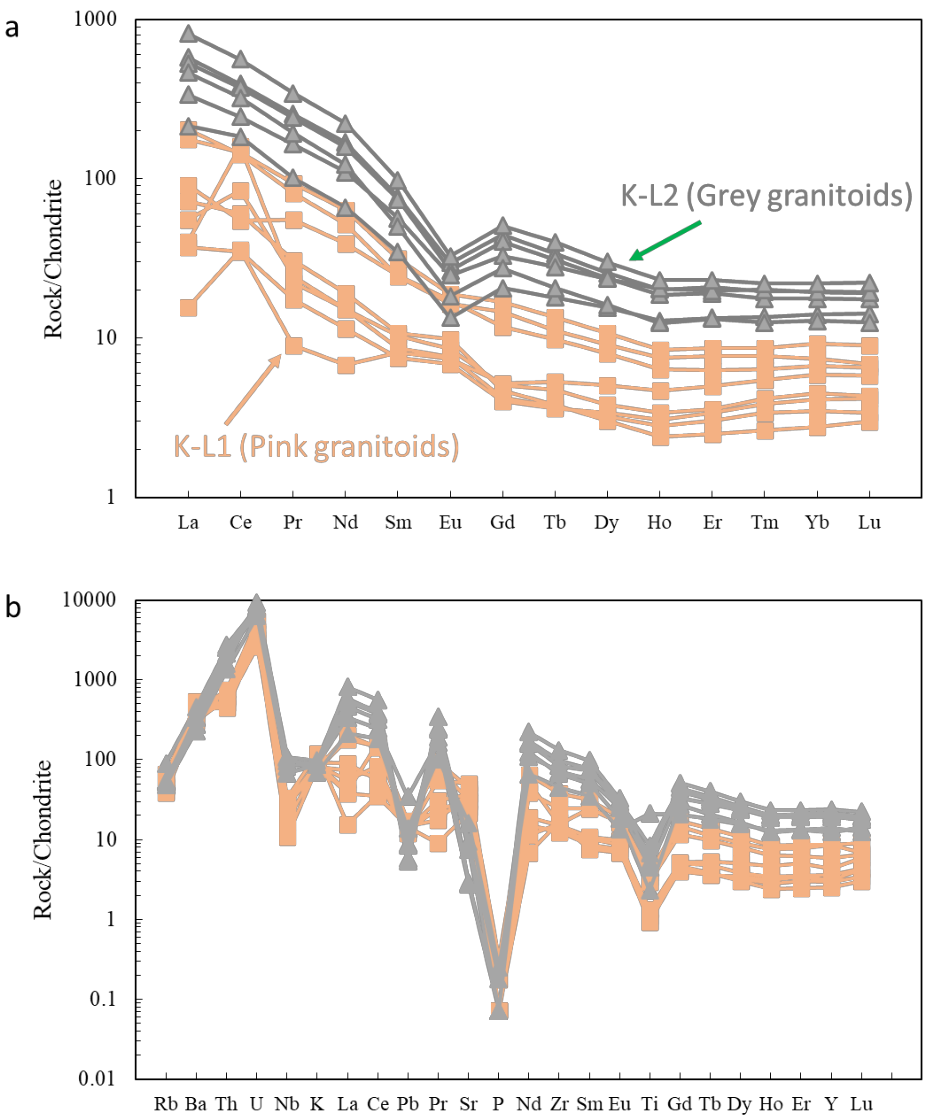

Fig. 4 Chondrite-normalized rare earth element (REE) diagram (a) and spider diagram (b) for weathered pink (K-L1) and grey (K-L2) granitoid samples. Normalization values from Sun and McDonough (1989). The prominent negative Eu anomaly and higher REE concentrations

in grey samples reflect weathering effects, whereas the overall REE and elemental patterns show similar trends between the two sample types.

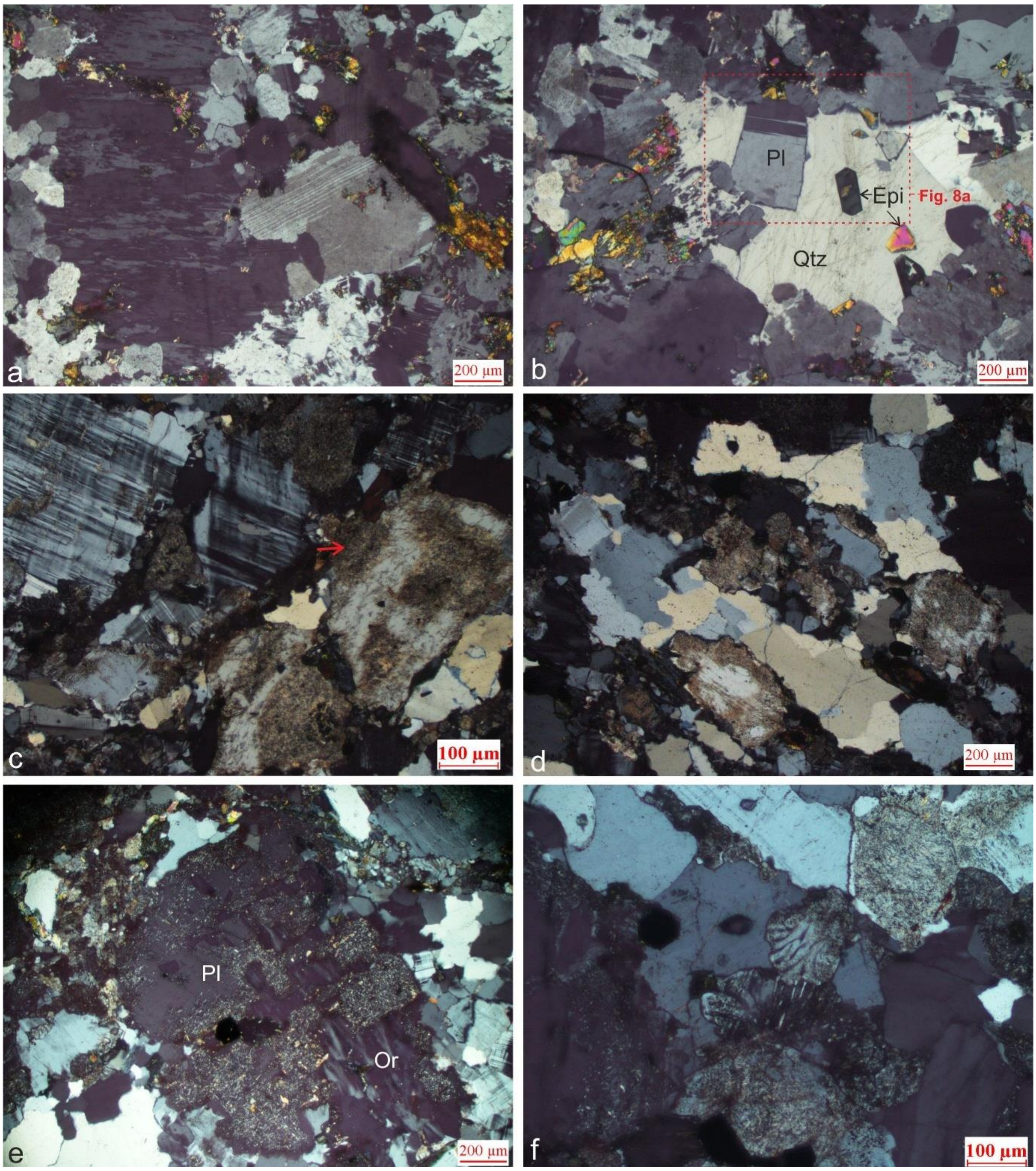

Fig. 5 Petrographic features of grey granite (a–b) and pink granite (c–f). (a) Very coarse perthite grain associated with weakly altered plagioclase. (b) Unaltered plagioclase showing lamellar twinning; note the occurrence of euhedral magmatic epidote enclosed within orthoclase. (c) Coarse microcline grains associated with highly altered plagioclase showing core alteration. (d) Inequigranular quartz associated with saussaritized plagioclase grains

showing rim alteration (black arrow) and complete alteration (red arrow). (e) Plagioclase partially altered to orthoclase with secondary sericite patches. (f) Myrmekitic texture along the contact between orthoclase and plagioclase feldspar.

4.3.2 Pink Granite

Notably the pink granite is same as the grey granite in mineral assemblage, except that it is characterized by a higher plagioclase each to K-feldspar ratio, relative to the grey granite. On the other hand, among the K-feldspars the abundance of microcline and microcline-microperthite is higher in the pink granite than in the grey granite (Fig. 5c). However, porphyroclasts of both K-feldspar and plagioclase are common in pink granite. It is noteworthy that in contrast to the least alteration of plagioclase, if any, in grey granite, most plagioclase grains in the pink granite are extensively saussuritized, often obscuring the lamellar twinning (Fig. 5d). Secondary minerals littered on surface of many plagioclase grains include sericite, epidote, iron oxides, and occasionally chlorite and K-feldspar (Fig. 5e). Different altered plagioclase grains show distinct distribution patterns of secondary minerals (section 4.3.4). Compositional zonation in individual plagioclase grain is defined by Ca-depleted altered domains made up of Ab_{95-100}, and Ca-rich unaltered zones with oligoclase to andesine compositions (Ab_{70-88}) (Table S2). Biotite grains are partially or completely altered to chlorite where secondary titanite grains are also present within the chlorite grains. Magnetite occurs as euhedral to subhedral blocky grains, often in close association with sericite. Myrmekitic textures are more abundant in pink granite relative to the grey variety (Fig. 5f).

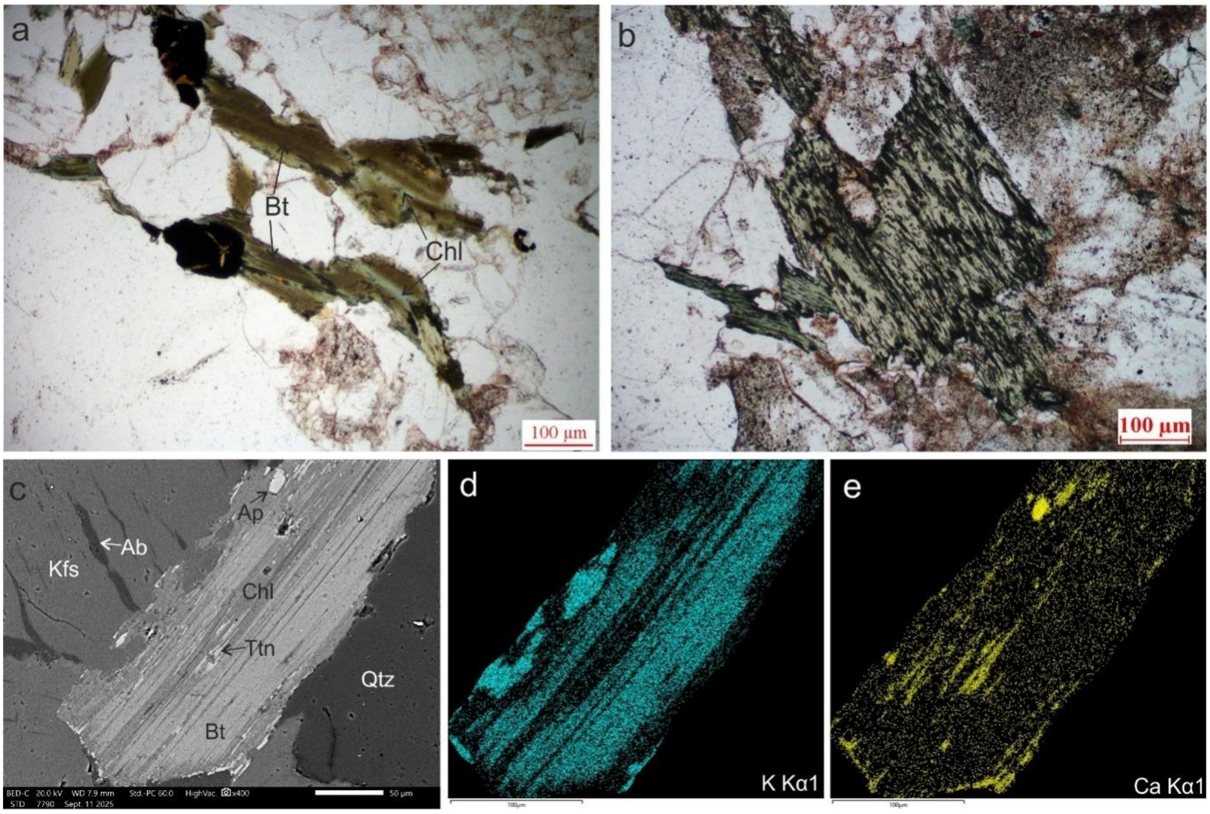

Fig. 6 Biotite alteration and secondary mineral development. (a) Partially altered biotite grains with secondary chlorite developed along cleavage planes. (b) Secondary chlorite completely replacing biotite grains. (c) SEM image showing secondary chlorite replacing biotite along the cleavage plane, with associated secondary titanite grains. (d–e) Elemental mapping of the biotite–chlorite association. (d) Elemental map showing K distribution (Kα1 line); note that chlorite-rich domains appear dark due to the absence of K. (e) Elemental map showing Ca distribution (Kα1 line); bright spots represent titanite.

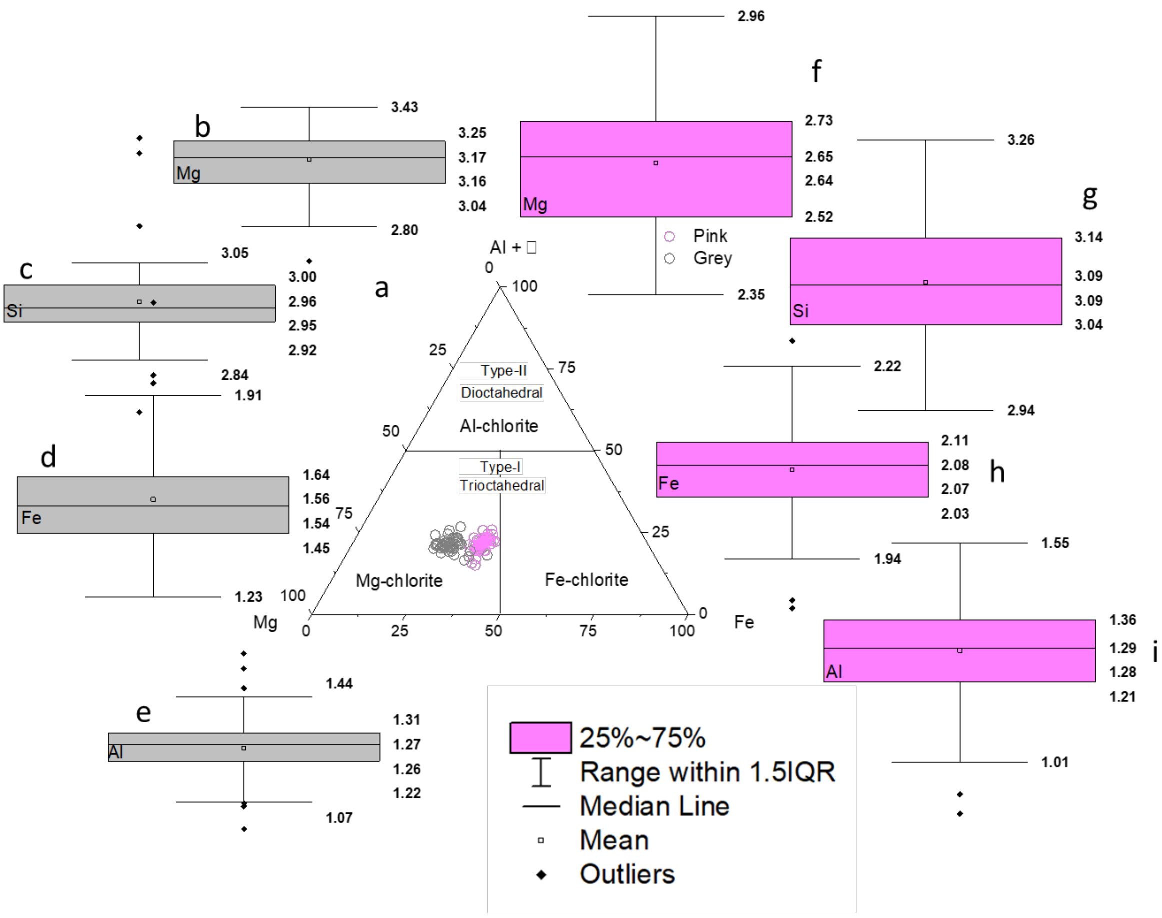

Fig. 7. Characterization of secondary chlorites. (a) Ternary compositional diagram (Al + vacancy – Mg – Fe; apfu) illustrating chlorites from pink and grey granitoids, where pink granitoid chlorites are notably richer in iron relative to those from grey granitoids.(b–e) Bar diagrams compare atom per formula unit (apfu) values for major cations (Mg, Fe, Al, Si) in chlorites from grey granitoids (N = 53), while (f–i) present those for pink granitoids (N = 53). Chlorites from pink granitoids display enrichment in Si and Fe and depletion in Mg, with Al remaining nearly constant across both groups.

4.3.3 Biotite-chlorite alteration

Chlorite occurs as two distinct textural varieties in both pink and grey granitoids of Bundelkhand. Chlorite usually coexist with biotite as interleaved flakes or individual flakes (Fig. 6a). At places, it occurs as pseudomorphous aggregate after biotite (Fig. 6b).In both varieties, titanite is ubiquitous as a common secondary mineral, occurring preferentially along cleavage planes of altered biotite. Less frequently apatite and K-feldspar are also observed as inclusions. Composition of chlorite can be classified into Type I (trioctahedral) and Type II (dioctahedral) categories based on octahedral cation occupancy determined from

SEM-EDS data (Fig. 7), with X_{Mg}+ X_{Fe} ≥ X_{Al} + $X_{Vacancy}$ for Type I and X_{Mg}+ X_{Fe}<X_{Al} + $X_{Vacancy}$ for Type II (Table S3). The apfu comparisons of the average chlorite compositions of grey and pink granitoids (Fig. 7) reveal that the secondary chlorites of pink granitoids are rich in iron and silicon and poor in magnesium in comparison to that of grey granitoids.

4.3.4 Plagioclase Alteration

The plagioclase grains in the Bundelkhand pink granites exhibit varied degree of alteration covering whole or part of the grains, whereas the plagioclase of grey granitoids are distinctively unaltered or very weakly altered. The altered plagioclases are represented by saussuritization products, i.e., a fine-grained assemblage of albite, K-feldspar, sericite, epidote, and iron oxides. Depending upon the distribution pattern of these secondary mineral products on individual grains it can be divided into four types (A, B, C, D). The petrographic analysis further reveals that plagioclase alteration patterns within the pink granitoids are fundamentally associated with micropore distribution and connectivity. These micropores, typically ranging from submicron to several micrometres in size, create interconnected networks that determine both the extent and spatial pattern of alteration within individual plagioclase crystals, as discussed below.

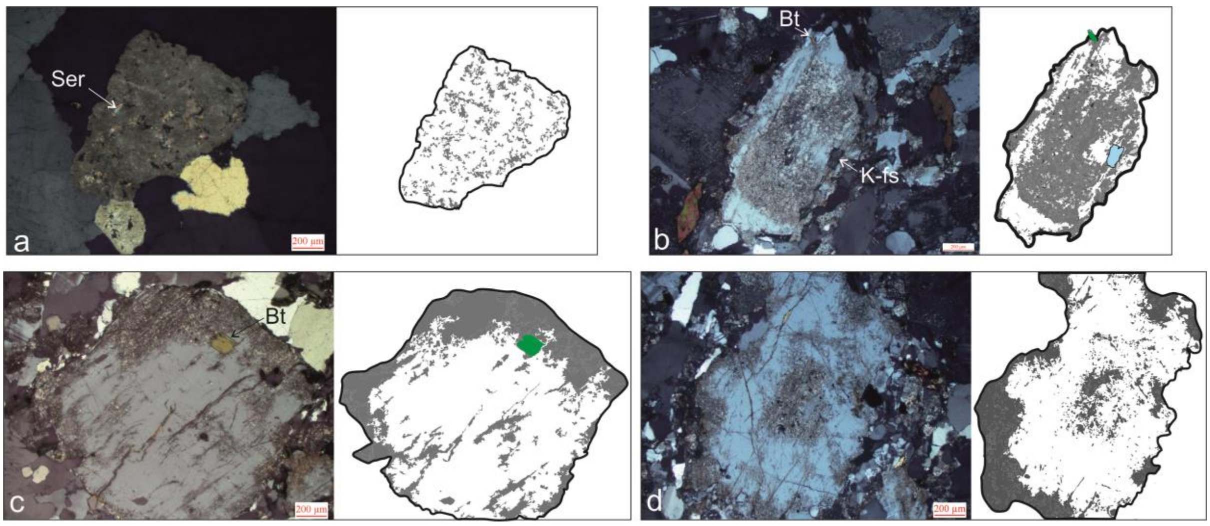

Fig. 8 Different types of plagioclase alteration patterns with line sketches in the right panel. (a) Plagioclase altered throughout the entire grain. (b) Core alteration of plagioclase with wide distribution from core to rim. (c) Rim alteration along the margin of plagioclase; note the inclusion of unaltered biotite within the plagioclase. (d) Both core and rim alteration in a single plagioclase grain.

Type A: Pervasive Alteration

The Bundelkhand pink granites display extensive Type A alteration, represented by almost complete alteration of plagioclase grains by the secondary minerals (Fig. 8a). The micropores, typically ranging in size from submicron to several micrometres, are evident in the plagioclase grains, which are filled up principally by sericite flakes.

Type B: Core Alteration

Type B alteration is represented by the secondary mineral assemblage restricted in the cores of plagioclase grains, while the marginal parts look clear (Fig. 8b). Under SEM it has become evident that the cores and rims of plagioclase grains with Type B alteration pattern are relatively Ca-rich and Na-rich respectively.

Type C: Rim Alteration

Type C alteration involves partial replacement of rims of the grains, while the cores remain clear. It typically occurs where the plagioclase grains are in contact with the chloritized-biotite (Fig. 8c). The inner boundaries of the rim alteration zones are usually irregular.

Type D: Zoned Alteration

Some plagioclase grains of the Bundelkhand pink granite display zoned alteration pattern which is being reported for the first time from this craton. It is characterized by alteration mineral assemblage at both the core and rim of a single grain, while preserving middle zone unaltered (Fig. 8d).

5. Discussion

Weathering profiles and fresh granitoid samples from the south-eastern Bundelkhand region provide critical insights into the petrogenetic relationships between different granite varieties and their alteration processes. This study examines weathered profile samples from Khajuraho to establish weathering trends among the pink, grey, and intermediate (mixed) Bundelkhand granitoids, demonstrating that pink-coloured domain represents K-metasomatic variants of grey granitoids (section 4.1). Subsequently, fresh pink and grey granitic samples from the south to south-eastern part of the Bundelkhand craton (Khajuraho, Chattarpur and Bijawar) are analysed to elucidate metasomatic alteration pathways (section 4.2), followed by examination of the regional extent of this alteration beyond the immediate study area (section 4.3), and finally consideration of the hypothesized nature and source of metasomatic fluids (section 4.4). These integrated analyses provide new understanding of K-metasomatic processes affecting Bundelkhand granitoids and their broader implications for regional granite petrogenesis.

5.1 Constraints from A-CN-K compositional space

The differential weathering rates of plagioclase and K-feldspar provide crucial insights into chemical weathering processes. Plagioclase characteristically weathers more rapidly than K-feldspar(Goldich 1938), driving predictable trends in the A-CN-K ternary diagram where weathering trajectories move away from the CN axis toward the A apex (Nesbitt et al. 1980). Algeo et al. (2025) identified four distinct weathering pathways reflecting varying degrees of feldspar alteration: (1) trends directed toward the AK axis represent selective dissolution of plagioclase without K-feldspar alteration, (2) trends toward the A apex indicate concurrent dissolution of both feldspars, (3) curved trajectories initially toward AK then deflecting to A represent sequential weathering beginning with plagioclase dissolution followed by K-feldspar alteration, and (4) trends initially toward ACN then curving to A reflect preferential retention of Ca and Na relative to K in paedogenic smectites.

However, metasomatic processes involving K, Na, or Ca addition can significantly perturb these ideal weathering trajectories, consequently alter CIA values and compromising the assessment of paleo-weathering intensity. The weathered Bundelkhand samples exhibit A-CN-K distributions that deviate markedly from the established weathering pathways described above (Fig. 3e). These patterns resemble those weathered signatures reported by Kanhaiya et al. (2018, 2024) in both bedload and weathered profile studies from the same region. However, Kanhaiya et al. (2018, 2024) neither decipher the different parent granitoid types nor explain the deviation of samples from ideal weathering trend.

Detailed examination of parent rock characteristics of the weathered profiles from the study area reveals contrasting weathering behaviours between lithological variants within the Bundelkhand terrain. Grey granitic samples (K-L2) follow conventional weathering trends characterized by progressive loss of mobile elements (Ca, Na, K) and retention of immobile Al (Figs 3c). Conversely, our pink granitic samples display compelling evidence of metasomatic modification characterized by systematic K enrichment at the expense of Ca and

Na depletion. The pink granite weathered samples define trajectories sub-parallel to the CN-K axis, consistent with 1:1 molar replacement of (CaO + Na_2O) by K_2O (Fig. 3a).

Such deviations from predicted weathering patterns result from K-metasomatism affecting the parent rock through two primary mechanisms: (1) conversion of aluminous clay minerals (kaolinite to illite) with addition of K from external source without replacement, and (2) replacement of plagioclase by authigenic K-feldspar, where the replacement can happen as 1:1 molar replacement of CaO + Na_2O by K_2O or replacement by any intermediate value. Both processes systematically increase K_2O content, causing samples to deviate from expected weathering trajectories and potentially leading to misinterpretation of paleoclimatic conditions. These processes can be represented by the following corrected and balanced chemical reactions:

XM1: $K^+ + 1.5\ Al_2Si_2O_5(OH)_4 \rightarrow KAl_3Si_3O_{10}(OH)_2 + H^+ + 1.5H_2O$

XM2: $CaNaAl_3Si_5O_{16} + K^+ \rightarrow KAlSi_3O_8 + CaAl_2Si_2O_8 + Na^+$

Plots in the A-CN-K ternary diagram demonstrate systematic K enrichment coupled with Ca and Na depletion in weathered pink granite profile samples (K-L1), closely resembling the XM2 hypothetical trend (Fig. 1b). Strong negative correlations between Ca-Na and K (excluding the surface sample from K-L1) support this interpretation (Fig. 1c). This geochemical signature indicates that Bundelkhand pink granites represent metasomatized derivatives of grey granite (cf. Sensarma et al.,2018; Rout et al.,2025).

Furthermore, sample distribution in the A-CNK-FM diagram (Fig. 3d) suggest that the grey granitoid weathered profiles exhibit normal weathering trends characterized by progressive loss of Ca, Na, and K, whereas pink granitoid weathered profiles display clustered compositions reflecting variable proportions of mafic components and feldspars (Fig. 3d). Notably, the Bundelkhand grey granitoids contain mafic components in higher proportions than pink granitoids, consistent with the characterization of grey granites as mafic-rich varieties by Bhattacharjee and Ahmad (2023) and Joshi et al. (2017). This observation directly contradicts the hypothesis proposed by Sensarma et al. (2018), who suggested that pink granites formed through high-temperature (950°C) alteration by Fe-Mg-Na-K-rich mafic fluids, linked to Paleoproterozoic dolerite dyke emplacement. If mafic fluid addition had occurred, pink granites would exhibit elevated Fe+Mg concentrations relative to grey granites. Therefore, the Fe-rich particles in altered feldspar observed in pink granites

(Sensarma et al. 2018), more likely resulted from internal alteration of pre-existing mafic phases such as biotite rather than external mafic fluid infiltration.

5.2 Pathways of alteration

As established above, the pink granitoids represent metasomatic altered product of grey granitoids. The successive stages of evolution of the distinctive characteristics of these two granitoid varieties are discussed as follow

5.2.1 Stage 1: Primary Driving Process – Biotite Chloritization

The most distinct characteristic of pink granitoids is altered plagioclase grains ~~(section 4.3.3)~~, which are found to be always associated with micropores and biotite chloritization. The plagioclase alteration patterns (Types C and D) clearly demonstrate that the alteration sequence initiated with biotite chloritization, which served as both the primary source of chemical components and the structural pathway for subsequent plagioclase modification. This observation is similar to that of Yuguchi et al. (2015, 2019), according to whom biotite chloritization provides essential components for downstream reactions. In the present studied samples, chlorite is commonly associated with biotite and titanite (Fig. 6), resembling the Type B-1 reaction as formulated by Yuguchi et al. (2015).

$$0.357\mathrm{Bt} + 0.362\ \mathrm{Al}^{3+} + 0.050\ \mathrm{Mg}^{2+} + 0.495\ \mathrm{Ca}^{2+} + 3.082\ \mathrm{H_2O} + 3.857\ \mathrm{H}^{+} \rightarrow 0.417\ \mathrm{Chl} + 0.495\ \mathrm{Ttn} + 1.478\ \mathrm{H_4SiO_4} + 0.158\ \mathrm{Fe}^{2+} + 1.469\ \mathrm{K}^{+} + 0.069\ \mathrm{F}^{-} + 0.015\ \mathrm{Cl}^{-}$$

The reaction liberates K^+, Fe^{2+}, H_4SiO_4 and other components into the hydrothermal fluid while consuming H^+ and H_2O, creating local geochemical environments conducive to plagioclase breakdown and establishing the chemical foundation for the metasomatic transformation of grey to pink granitoids. The presence of titanite in the secondary chlorite, along the cleavage of the original biotite flakes (Fig. 6c), supports the above reaction. Interestingly, this alteration pattern was observed in both the grey and pink granitoid samples. The compositions of chlorites in both these varieties were classified as Type-I Mg chlorites, where the chlorites of pink granitoids were systematically higher in the Ternary compositional diagram (Fig. 7) than that of the grey granitoids. The decrease in Mg content of the chlorites in the pink granitoids than their grey counterparts (Fig. 7) supports that the pink granitoids are more hydrothermally altered than grey granitoids (Parry and Downey 1982).

5.2.2 Stage 2: Micropore Formation Through Anorthite Dissolution

Plagioclase alteration patterns in the Bundelkhand granitoids reveal compositional and microstructural controls on alteration susceptibility. The most striking microscopic feature is the clouded plagioclase in pink granitoids, contrasting sharply with the relatively unaltered plagioclase in grey granitoids. This distinction arises from fundamental compositional differences: plagioclase in grey granitoids is Na-rich (albitic), whereas plagioclase in pink granitoids is Ca-rich (oligoclase). Because Ca-rich plagioclase is considerably more susceptible to hydrothermal alteration than its Na-rich counterpart (Yuguchi et al. 2019), the clouded texture of pink granitoid plagioclase reflects the development of micropores filled dominantly with sericite and iron-oxides. This observation is consistent with that of Que and Allen (1996), who have shown that the micropores form during the initial stage of alteration facilitate hydrothermal fluid infiltration into plagioclase grains, promoting further alteration progression. Further, Yuguchi et al. (2019) quantified this feedback mechanism, demonstrating that micropores generated through anorthite dissolution create interconnected pathways that enable deeper fluid penetration and sustained alteration. The characteristic cloudy texture and abundant micropore networks in pink granitoid plagioclase directly reflect this progressive alteration process.

This alteration pattern also explains the patchy nature of the grey granitoids in Bundelkhand. The grey granitoids occur within the dominant pink granitoid of the studied region, which could result from two complementary factors: (i) Na-rich plagioclase exhibits inherently lower susceptibility to alteration compared to Ca-rich plagioclase, and (ii) fluid chemistry evolution toward higher pH through chloritization (Section 4.2.1) reduces alteration potential. The consumption of H^+ ions during chlorite formation raises pH, decreasing the corrosivity of the hydrothermal fluid and limiting further plagioclase breakdown. Enhanced porosity and extensive interconnected micropore networks in pink granitoids reflect the cumulative extent of fluid-rock interaction, with these microporous textures serving as direct records of prolonged anorthite dissolution and sustained hydrothermal activity.

5.2.3 Stage 3: Sequential Albitization and K-Feldspathization

Following micropore formation, plagioclase underwent systematic replacement through coupled dissolution-reprecipitation reactions that are strictly controlled by micropore distribution. The plagioclase grains of grey granitoids are relatively Ca-poor and contain less micropores as compared to that of the pink granitoids (Fig. 9c). Research has consistently demonstrated that both sericite occurrence and plagioclase compositional changes are strictly controlled by the distribution of micropores in plagioclase grains (Morad et al. 2010), with areas free of micropores remaining impermeable to alteration fluids and staying fresh and unaltered. This principle applies directly to the Bundelkhand grey granitoids, which show minimal alteration due to limited micropore development (Fig. 9c).

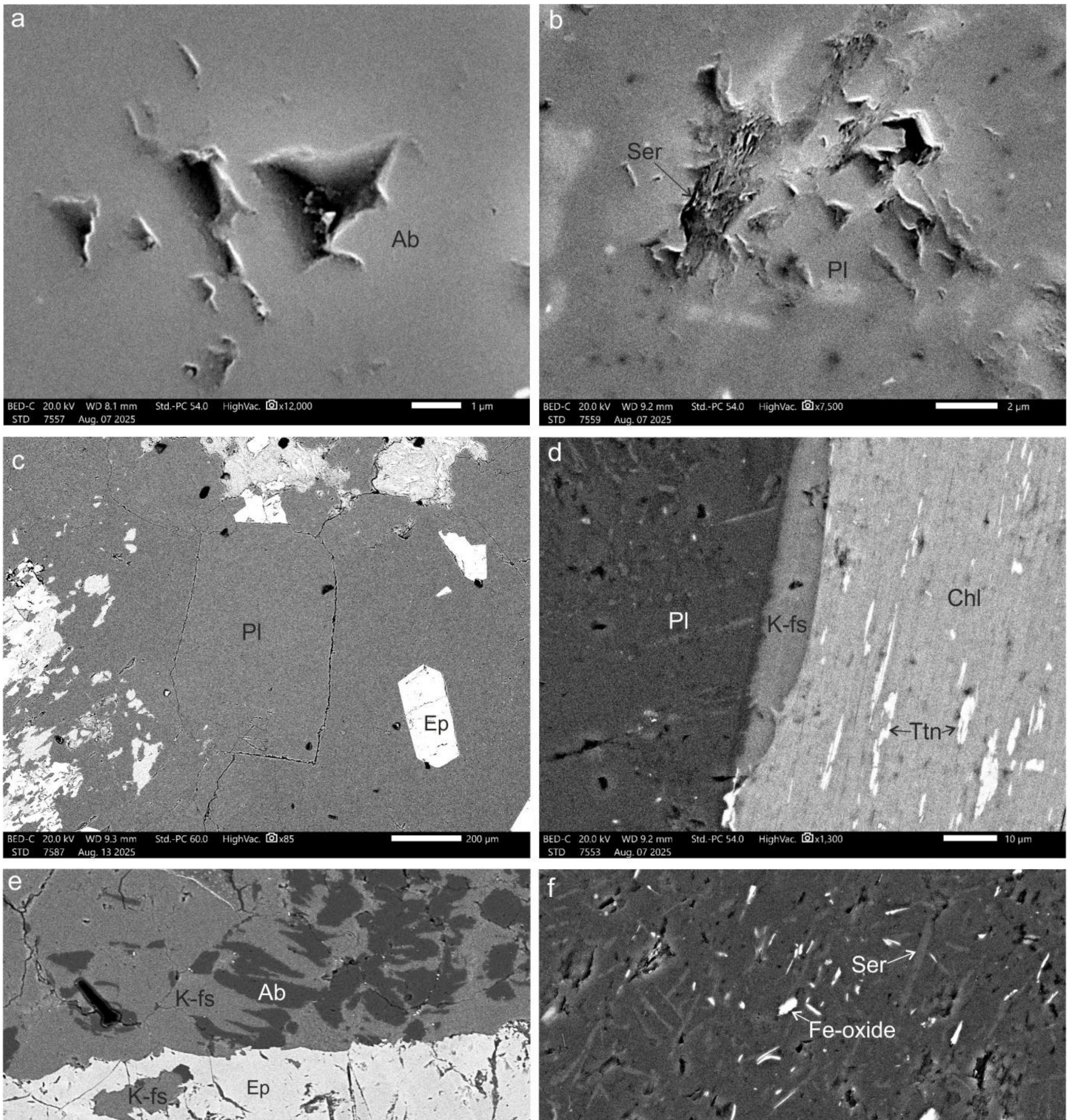

Fig. 9 SEM observations of feldspar alteration and secondary mineral development. (a) Secondary electron (SE) image showing triangular-shaped vacant microspores within plagioclase of grey granitoid. (b) SE image of sericite development within micropores in plagioclase grains of pink granitoid. (c) SE image of completely unaltered albite and euhedral magmatic epidote from grey granitoid. (d) K-feldspathization along the contact between plagioclase and chlorite within pink granitoid; note the secondary chlorite formed from biotite alteration. (e) Late-stage epidote veins crosscutting feldspar grains, indicating fluid pathways. (f) Very small iron oxide and sericite inclusions within plagioclase feldspar.

The process involves direct K-feldspathization utilizing K^+ released from biotite chloritization (Fig. 9d):

$$NaAlSi_3O_8 + K^+ \rightarrow KAlSi_3O_8 + Na^+$$

$$CaAl_2Si_2O_8 + 2K^+ \rightarrow 2KAlSi_3O_8 + Ca^{2+}$$

This 1:1 molar exchange represents the diagnostic reaction for the metasomatic transformation and accounts for the sub-parallel trajectory observed in A-CN-K ternary diagram for the Bundelkhand pink granitoids, where K_2O systematically increases at the expense of (CaO + Na_2O) (Fig. 3a). Identical K-feldspathization processes have been documented in the Swedish granites (Morad et al., 2010), where the secondary feldspars replace magmatic plagioclase and are most abundant in red-stained granitic rocks that occur as zones adjacent to fractures.

5.2.4 Stage 4: Sericite Formation and Mass Transfer

Concurrent with K-feldspathization, sericite formation occurred within the microporous framework through reaction of hydrothermal fluids with pore walls (Fig. 9b). The K^+ ion generated from stage 1 from the chloritization of biotite was the probable source of ion for the formation of sericite (Que and Allen 1996; Morad et al. 2010). Most of the sericite observed in the present study are K bearing with few Fe in their structure. A simplified balanced reaction for sericite formation is:

$$3NaAlSi_3O_8 + K^+ + 2H^+ \rightarrow KAl_3Si_3O_{10}(OH)_2 + 3SiO_2 + 3Na^+$$

This reaction produces fine-grained muscovite within the microporous domains, contributing to the characteristic sericitized appearance of altered plagioclase cores while leaving the micropore-free margins unaltered.

5.2.5 Stage 5: Epidote Precipitation and Calcium Mass Balance

Concurrent with feldspar alteration, epidote precipitated consuming Ca^{2+} and Al^{3+} released during plagioclase dissolution, with both grey and pink granitoids containing epidote veins that indicate widespread fluid circulation (Fig 8e). The composition of secondary epidotes in both the pink and grey granitoids are given in Table S2. A simplified balanced reaction for epidote formation is:

$$2Ca^{2+} + 2Al^{3+} + Fe^{3+} + 3SiO_2 + H_2O \rightarrow Ca_2Al_2Fe^{3+}Si_3O_{12}(OH) + 6H^+$$

This reaction consumes excess Ca^{2+} from plagioclase breakdown and Fe^{3+} from chloritization while contributing to acidification of the hydrothermal fluid, promoting continued dissolution reactions and creating the characteristic epidote-lined micro-veins observed throughout both the Bundelkhand granite varieties. The composition of metasomatic epidotes were found to be dominantly Fe-rich (pistacite), which is an indication of low formation temperature (≤ 350 ºC) and elevated fO_2 (Morad et al. 2010 and references therein).

5.2.6 Stage 6: Iron Oxide Formation and Pink Coloration of Feldspar

The distinctive pink coloration resulted from iron-oxide precipitation within microporous altered feldspars, where iron derived from biotite chloritization underwent oxidation within the altered framework. This process is fundamentally controlled by micropore distribution, occurring preferentially in areas with high pore density (Fig. 9f). Morad et al. (2010) documented identical processes in Swedish granites, noting that the pervasively albitized plagioclase crystals were vacuolated and contained variable amounts of Fe-oxide pigment, inducing turbid appearance and red staining. The balanced for hematite formation reaction is:

$$4Fe^{2+} + O_2 + 4H_2O \rightarrow 2Fe_2O_3 + 8H^+$$

The hematite precipitates as submicron particles (typically <1 μm) dispersed throughout the altered feldspar matrix, creating the pervasive pink-red coloration that characterizes our metasomatized granite.

Therefore, the origin of pink coloration (or reddening) of the Bundelkhand granitoids can be attributed to the internal cycling of Fe through a fluid of silicic composition, rather than having any link to the dyke swarm of the Bundelkhand craton.

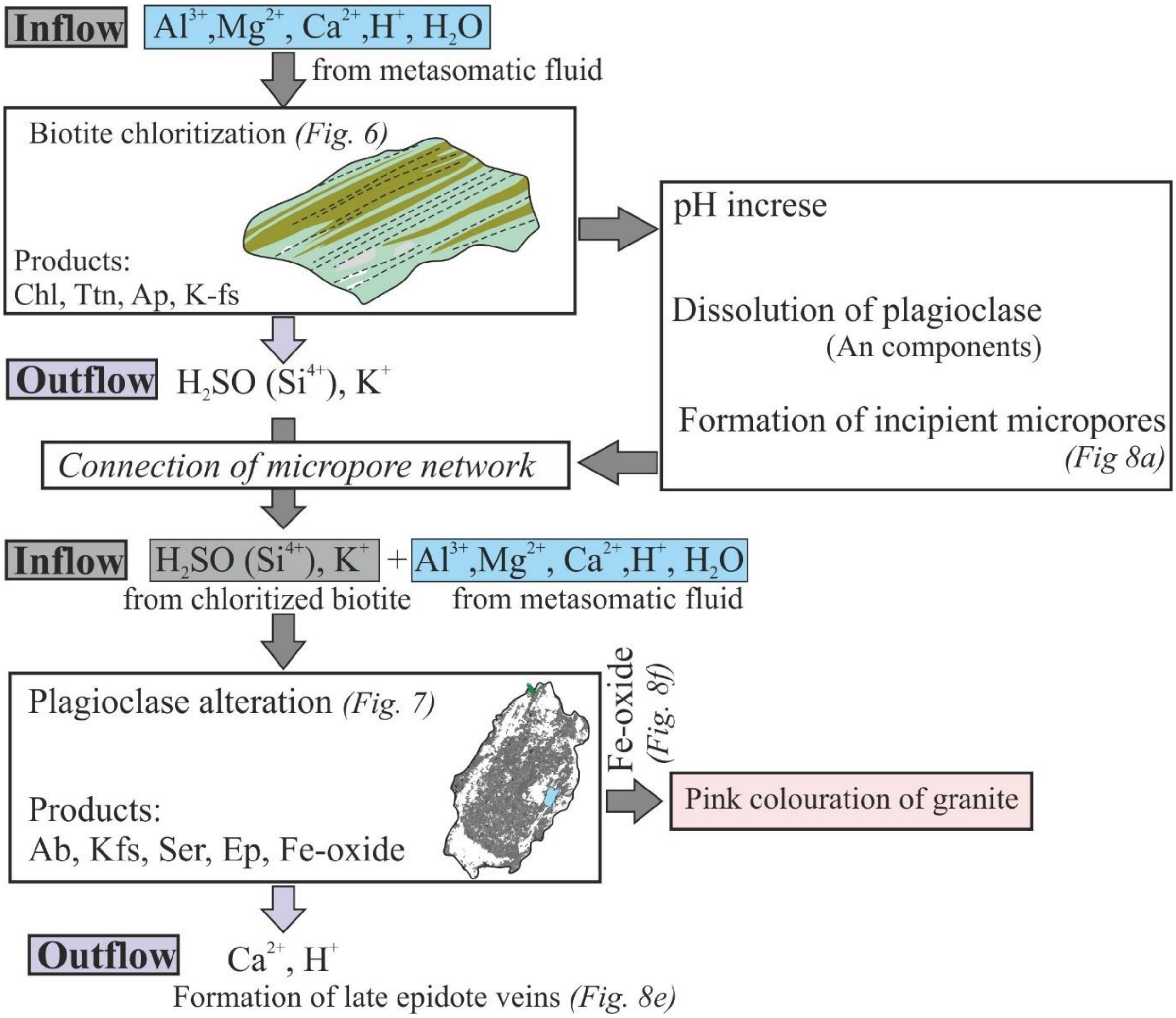

Fig. 10 Schematic representation of mass transfer of chemical constituents responsible for the pink coloration of Bundelkhand granite via metasomatic fluids during sequential alteration processes: biotite chloritization followed by plagioclase alteration (after Yuguchi et al., 2015, 2019, 2022).

5.3 Validation of Metasomatic process in entire craton

Though the weathered samples described above were primarily collected from the Khajuraho region, it is important to emphasize that the microstructural features, mineralogical assemblages, and alteration pathways detailed herein for pink granitoids are representative of broader regional processes. These characteristics are evident in samples collected from

Chattarpur, Khajuraho, and Bijawar localities that together constitute the southeastern part of the Bundelkhand craton.

Multiple previous investigations across the Bundelkhand granitoid terrain have independently documented the same diagnostic features, including: (i) systematic K-enrichment coupled with Na-Ca depletion, (ii) extensive sericitization of plagioclase cores associated with micropore development, (iii) pervasive biotite chloritization providing internal sources of Fe and K, and (iv) widespread occurrence of pink-coloured granite variants dominating over grey counterparts throughout the craton. These observations, summarized and expanded in Table A1 below, strongly corroborate the specific pathways of metasomatic alteration elucidated in this study.

The regional-consistency of these alteration characteristics despite minor local lithological or structural variations, validates the above-proposed alteration pathways and mechanistic models. Therefore, pink granitoids universally represent the product of a pervasive hydrothermal metasomatic overprint on grey granitoids, rather than constituting an independent magmatic episode. The concurrent crystallization ages of ~2.5 Ga, as reported from high-precision U-Pb zircon and monazite geochronology across Bundelkhand granitoids (Ray et al. 2016; Slabunov and Singh 2022; Joshi et al. 2022), further attest to this genetic relationship, indicating synchronous emplacement followed by regionally extensive alteration processes.

The chondrite-normalized REE patterns of the weathered pink and grey granitoids also demonstrate similar REE fractionation characteristics, exhibiting enrichment in light rare earth elements (LREE) and depletion in heavy rare earth elements (HREE). The $(La/Yb)_N$ ratios, which quantify REE fractionation, show similar overlapping relationships between both granite varieties, indicating a common source and similar petrogenetic processes. However, the systematically higher REE concentrations observed in grey granitoids compared to pink varieties can be attributed to enhanced chemical weathering intensity in grey samples, which concentrates REEs in the residual weathered products. This pattern is consistent with established principles of REE behaviour during granite weathering, where REEs tend to accumulate in weathering profiles due to their low mobility and preferential retention in secondary clay minerals. The primitive mantle-normalized multi-element spider diagrams for both sample sets also exhibit similar trends, characterized by enrichment in large ion lithophile elements (LILE) such as Rb, Ba, and K, and depletion in high field strength elements (HFSE) including Nb, and Ti. These geochemical signatures are diagnostic of crust-derived melts and further support the interpretation that both grey and pink varieties represent similar source materials.

5.4 Nature and Evolution of Fluid

The above discussion (sections 4.1, 4.2 and 4.3) conclusively demonstrates that the pink granitoids represent metasomatized derivatives of grey granitoids, and hence both granitoid varieties are genetically linked and formed from a single magmatic pulse and tectonic episode. Hence, this works convincingly explain the reason for the same age recorded for both these varieties in multiple studies (Kaur et al. 2016; Joshi et al. 2022 and references therein). Further, it has also been demonstrated that the reacting fluid composition is poor in Fe concentration and hence, unlikely to be a derivative of mafic dyke swarm as earlier speculated by Sensarma et al. (2018). Sensarma et al. (2018) suggested that mafic-derived fluids traversed through green-coloured veins (of unidentified mineralogy) and caused the pink coloration in Bundelkhand granitoids. This mechanism would require systematic alteration gradients adjacent to the veins; however, the observed spatial and microstructural relationships between pink and grey granitoids do not support such a model. The green-coloured material has been identified as epidote-group minerals, representing a product of alteration (section 5.2.5) rather than the fluid source. Fluid migration pathways have been established as predominantly micropores within plagioclase crystals (section 5.2.2), consistent with pervasive metasomatism rather than vein-controlled fluid flow.

Though, without comprehensive fluid inclusion or thermometry studies, it is not possible to establish the precise nature and hence compositional evolution of fluid that caused the above-mentioned metasomatism, the chlorite composition determined through EDS and the mineralogical associations within granitoids observed in the present study, can be used to infer the temperature and chemical nature of the alteration fluid. Since, the chlorite in these granitoids represent late-hydrothermal phase, the temperature estimations derived from its mineral chemistry denote the temperature regimes of the late-stage fluid. Numerous studies (Cathelineau and Nieva 1985; Cathelineau 1988; Bourdelle 2021 and references therein) have highlighted the increase in Al^{IV} and the decrease in octahedral vacancies in chlorites with increasing temperature.

In the present study, a series of temperatures were calculated for both the grey and pink granitoid samples using 14 oxygens basis through the WinCcac program (Supplementary file

1-Table S3). The average of the temperature estimations based on Al^{IV} content (Cathelineau and Nieva 1985; Kranidiotis and MacLean 1987; Cathelineau 1988; Jowett 1991; Zang and Fyfe 1995; Xie et al. 1997) showed a small difference of ~40 ºC between the grey (216 ± 19 ºC, n= 53) and pink granitoids (257 ± 25 ºC, n=53). Though, these thermometers are empirical in nature, the closer values in the pink and grey granitoid samples of the present study highlight the alteration through a similar event via common fluid reaction with biotite, where the alteration of grey granitoids are comparatively earlier and in a high temperature regime than that of the pink granitoids. This is also consistent with the lower concentration of Mg in chlorites of pink granitoids as compared to that of the grey variety (Figs. 7b and 7f), which indicate that the alteration of biotite in pink is more pronounced (Parry and Downey 1982). The presence of chlorite and titanite as an alteration assemblage of biotite (section 4.3.1) generally occurs at a temperature range of 290° to 350°C (Yuguchi et al. 2015). The mineralogical modifications encountered agree well with the precipitation temperature range of ca. 250–400°C deduced by hydrothermal alteration studies in similar granitic systems (Morad et al. 2010). The Fe-rich composition of the secondary epidote suggests formation temperatures of ≤350°C, under elevated fO_2 and low PCO_2 conditions (Liou 1973; Liebscher and Franz 2004). Experimental studies have demonstrated that epidote composition becomes more Fe-rich with increasing oxygen fugacity, with maximum Fe^{3+} content occurring at high oxygen buffers (hematite-magnetite) and more aluminous compositions at lower fO_2 values (Liebscher and Franz 2004). The presence of hematite within chloritized-biotite supports elevated oxygen fugacity in the hydrothermal fluids. This observation is further supported by the systematic occurrence of chlorite + titanite + epidote + sericite assemblages, which indicate interaction with oxidizing, low-salinity hydrothermal fluids. The absence of significant sulphide mineralization and the predominance of oxide phases (hematite, titanite) support relatively oxidized fluid conditions. The internal source of Fe from biotite breakdown, coupled with the felsic character of the metasomatic fluids, suggests derivation from late-stage magmatic fluids rather than external meteoric or basinal brines.

Comparison with similar granite-hosted hydrothermal systems worldwide indicates that the observed mineral assemblages and alteration patterns are consistent with sub-solidus cooling and fluid exsolution from the crystallizing granite pluton. The temperature range of 250°-400°C inferred from mineral assemblages corresponds to the typical range for post-magmatic hydrothermal systems in granitic environments. Therefore, the combined mineralogical and geochemical evidences collectively suggest that the metasomatic fluids responsible for the grey-to-pink granite transformation were internally derived, oxidizing hydrothermal solutions that operated during post-magmatic cooling at temperatures between 200-400°C. This interpretation is consistent with the genetic relationship between grey and pink granitoids and supports a single-event origin for both the varieties.

5. Conclusions

Based on bulk major and trace element geochemistry of weathered samples from three profiles, the present study demonstrates that the pink (red) coloration of Bundelkhand granitoids represents metasomatic alteration of original grey granitoids, thus explaining the apparent dilemma in previous studies concerning identical radiogenic ages for both the varieties. The iron-rich character of grey granitoids compared to their metasomatic pink counterparts challenges the previous hypothesis of mafic-rich alteration fluids.

Biotite chloritization has been identified as the primary driving mechanism for a series of interconnected alteration processes, including albitization, sericitization, secondary epidote formation, and hematite precipitation in pink granitoids. The similar biotite-chloritization patterns observed in both the grey and pink granitoids demonstrates the pervasive nature of the alteration fluid. Temperature conditions based on chlorite thermometry and textural evidence indicate shallow crustal conditions (~200-350°C).

The dominance of micropores developed in pink granites through calcic-plagioclase alteration acts as conduits for metasomatic fluid migration across the vast Bundelkhand terrain without requiring dominantly associated secondary structural deformation features such as veins. The prevalence of Na-plagioclase and changes in altering fluid physicochemical conditions are interpreted as controlling factors that delimited alteration zones in some granitoid samples, which maintained grey coloration despite biotite-chloritization. This study establishes a novel pathway linking weathered chemistry with metasomatic alteration and demonstrates unambiguously that the granitoid chemistry of this Archean window predominantly represents a metasomatic alteration product.

Acknowledgement

The authors acknowledge technical support and laboratory facilities provided by the UGC-Centre for Advanced Study (CAS) and DST-Fund for Improvement of S&T Infrastructure

(FIST) programs at the Department of Geology, Presidency University, Kolkata. A portion of this work was conducted as part of the MSc thesis of AB.

Author contributions:

Shiba Shankar Acharya and Arnab Sain contributed to the study conception and design. All authors contributed to sampling, analytical measurements, and data analysis. Shiba Shankar Acharya and Arnab Sain wrote the first draft of the manuscript, and all authors provided critical comments on previous versions. All authors read and approved the final manuscript.

Funding:

AS and SSA acknowledge funding from the Anusandhan National Research Foundation (ANRF) [SUR/2022/002544].

Conflict of interest:

The authors have no relevant financial or non-financial interests to disclose.

Appendix A1:

Summary of documented alteration features and processes in Bundelkhand pink granites (with key literature)

Characteristics	Locations	Interpretations	References
Pervasive pink over grey granitoids	Throughout Craton	Grey granite altered to pink granite due to mafic fluid interaction	Sensarma et al., 2018
	Throughout Craton	Grey granite altered to pink granite due to fluid activity	Rout et al., 2025
	SW part of the Craton	Separate magma emplaced in coeval time	Bhattacharya & Ahmad, 2023
	Central part of Craton	Separate magma emplaced in coeval time	Kaur et al., 2016
	Southern part of the Craton	Separate magma emplaced in coeval time	Roy et al., 2016
Proportion of altered feldspar higher in pink granite	Throughout Craton		Sensarma et al., 2018
Grey granite rich in Na-feldspar (Albite)	Southern part of the Craton		Roy et al., 2016
Biotite to chlorite alteration	Throughout Craton		Sensarma et al., 2018
	Throughout Craton		Raut et al., 2025
	SW part of the Craton	Formed due to fluid activity	Bhattacharya & Ahmad, 2023
	Central part of the craton		Kaur et al., 2016
Extensive sericitization	Throughout Craton	Feldspar alteration	Sensarma et al., 2018
	Throughout Craton		Raut et al., 2025
	SW part of the Craton	Formed due to hydrothermal activity	Bhattacharya & Ahmad, 2023
	Central part of Craton		Kaur et al., 2016
	SE part of Craton	Hydrothermal metasomatism	Sanyal et al., 2025
	Central part of the Craton		Kumar et al., 2021
	Central and NW part of the Craton		Joshi et al., 2021
Albitization and K-Feldspathization	Throughout Craton		Sensarma et al., 2018
	Central part of the Craton	Gradual replacement of plagioclase by K-feldspar	Kaur et al., 2016
	Central part of the Craton		Kumar et al., 2021

Secondary epidote formation	Throughout Craton		Sensarma et al., 2018
	Throughout Craton	late hydrothermal fluid activity	Rout et al., 2025
Hematite inclusions within altered plagioclase	Throughout Craton		Sensarma et al., 2018

References

Algeo TJ, Hong H, Wang C (2025) The chemical index of alteration (CIA) and interpretation of ACNK diagrams. Chemical Geology 671:122474. https://doi.org/10.1016/j.chemgeo.2024.122474

Basu AK (1986) Geology of Bundelkhand granite massif, Central India. Records Geological Survey of India 101:61–124

Bhattacharjee J, Ahmad T (2023) Geochemistry and petrogenesis of Neoarchaean Granitoids from the southwestern Bundelkhand Craton: Implications on Archaean geodynamic evolution. J Earth Syst Sci 132:. https://doi.org/10.1007/s12040-023-02159-1

Boone GM (1969) Origin of Clouded Red Feldspars; Petrologic Contrasts in a Granitic Porphyry Intrusion. American Journal of Science 267:633–668. https://doi.org/10.2475/ajs.267.6.633

Bourdelle F (2021) Low-Temperature Chlorite Geothermometry and Related Recent Analytical Advances: A Review. Minerals 11:130. https://doi.org/10.3390/min11020130

Cathelineau M (1988) Cation site occupancy in chlorites and illites as a function of temperature. Clay Minerals 23:471–485. https://doi.org/10.1180/claymin.1988.023.4.13

Cathelineau M, Nieva D (1985) A chlorite solid solution geothermometer the Los Azufres (Mexico) geothermal system. Contr Mineral and Petrol 91:235–244. https://doi.org/10.1007/BF00413350

Deb T, Bhattacharyya T (2022) The evolution of the fracture systems under progressive sinistral shear in the Bundelkhand Craton, Central India: A review and new insights. Earth-Science Reviews 235:104238. https://doi.org/10.1016/j.earscirev.2022.104238

Fedo CM, Wayne Nesbitt H, Young GM (1995) Unraveling the effects of potassium metasomatism in sedimentary rocks and paleosols, with implications for paleoweathering conditions and provenance. Geology 23:921. https://doi.org/10.1130/0091-7613(1995)023%253C0921:UTEOPM%253E2.3.CO;2

Goldich SS (1938) A Study in Rock-Weathering. The Journal of Geology 46:17–58. https://doi.org/10.1086/624619

Jhingran AG (1958) The problem of Bundelkhand granites and gneisses. Presidential Address. Madras

Joshi KB, Bhattacharjee J, Rai G, et al (2017) The diversification of granitoids and plate tectonic implications at the Archaean–Proterozoic boundary in the Bundelkhand Craton, Central India. SP 449:123–157. https://doi.org/10.1144/SP449.8

Joshi KB, Singh SK, Halla J, et al (2022) Neodymium Isotope Constraints on the Origin of TTGs and High-K Granitoids in the Bundelkhand Craton, Central India: Implications for Archaean Crustal Evolution. Lithosphere 2022:. https://doi.org/10.2113/2022/6956845

Jowett EC (1991) Iron and Magnesium into the Hydrothermal Chlorite Geothermometer. In: In Proceedings of the GAC/MAC/SEG Joint Annual Meeting. Toronto, ON, Canada,

Kanhaiya S, Singh BP, Mittal P, Patra A (2024) Regolith profiles developed from a granitic parent rock in a sub-humid climate: implications for pedogenesis and chemical mobility of elements. J Sediment Environ 9:63–79. https://doi.org/10.1007/s43217-023-00157-3

Kanhaiya S, Singh BP, Singh S (2018) Mineralogical and Geochemical Behavior of Sediments Solely Derived from Bundelkhand Granitic Complex, Central India: Implications to Provenance and Source Rock Weathering. Geochem Int 56:1245–1262. https://doi.org/10.1134/S0016702918120054

Kaur P, Zeh A, Chaudhri N, Eliyas N (2016) Unravelling the record of Archaean crustal evolution of the Bundelkhand Craton, northern India using U–Pb zircon–monazite ages, Lu–Hf isotope systematics, and whole-rock geochemistry of granitoids. Precambrian Research 281:384–413. https://doi.org/10.1016/j.precamres.2016.06.005

Kranidiotis P, MacLean WH (1987) Systematics of chlorite alteration at the Phelps Dodge massive sulfide deposit, Matagami, Quebec. Economic Geology 82:1898–1911. https://doi.org/10.2113/gsecongeo.82.7.1898

Kumar G, Kumar S, Yi K (2021) Three distinct Archean crustal growth events as recorded from 3.48 Ga migmatite, 2.70 Ga leucogranite, and 2.54 Ga alkali granite in the Bundelkhand Craton, Central India. Journal of Asian Earth Sciences 219:104886. https://doi.org/10.1016/j.jseaes.2021.104886

Liebscher A, Franz G (2004) Epidotes. Mineralogical Society of America

Liou JG (1973) Synthesis and Stability Relations of Epidote, Ca2Al2FeSi3O12 (OH). J Petrology 14:381–413. https://doi.org/10.1093/petrology/14.3.381

Malviya VP, Arima M, Pati JK, Kaneko Y (2006) Petrology and geochemistry of metamorphosed basaltic pillow lava and basaltic komatiite in the Mauranipur area: subduction related volcanism in the Archean Bundelkhand craton, Central India. Journal of Mineralogical and Petrological Sciences 101:199–217. https://doi.org/10.2465/jmps.101.199

Malviya VP, Arima M, Verma SK, et al (2022) Petrology and geochemistry of the Palaeo-Mesoarchean Banded Iron formations (BIFs) from the central Bundelkhand greenstone belts, Bundelkhand Craton, India: Source characteristics and depositional environment. Geological Journal 57:3292–3312. https://doi.org/10.1002/gj.4471

McLennan SM (1993) Weathering and Global Denudation. The Journal of Geology 101:295–303

Mondal MEA, Goswami JN, Deomurari MP, Sharma KK (2002) Ion microprobe 207Pb/206Pb ages of zircons from the Bundelkhand massif, northern India: implications for crustal evolution of the Bundelkhand–Aravalli protocontinent. Precambrian Research 117:85–100. https://doi.org/10.1016/S0301-9268(02)00078-5

Morad S, El-Ghali MAK, Caja MA, et al (2010) Hydrothermal alteration of plagioclase in granitic rocks from Proterozoic basement of SE Sweden. Geological Journal 45:105–116. https://doi.org/10.1002/gj.1178

Nakano S, Akai J, Shimobayashi N (2005) Contrasting Fe-Ca distributions and related microtextures in syenite alkali feldspar from the Patagonian Andes, Chile. Mineral mag 69:521–535. https://doi.org/10.1180/0026461056940268

Nesbitt HW, Markovics G, price RC (1980) Chemical processes affecting alkalis and alkaline earths during continental weathering. Geochimica et Cosmochimica Acta 44:1659–1666. https://doi.org/10.1016/0016-7037(80)90218-5

Nesbitt HW, Young GM (1982) Early Proterozoic climates and plate motions inferred from major element chemistry of lutites. Nature 299:715–717. https://doi.org/10.1038/299715a0

Panigrahi MK, Mookherjee A (1997) The Malanjkhand copper (+ molybdenum) deposit, India: mineralization from a low-temperature ore-fluid of granitoid affiliation. Mineral Deposita 32:133–148. https://doi.org/10.1007/s001260050080

Parry WT, Downey LM (1982) Geochemistry of Hydrothermal Chlorite Replacing Igneous Biotite. Clays and clay miner 30:81–90. https://doi.org/10.1346/CCMN.1982.0300201

Pati JK (2020) Evolution of Bundelkhand Craton. Episodes 43:69–87. https://doi.org/10.18814/epiiugs/2020/020004

Pati JK, Patel SC, Pruseth KL, et al (2007) Geology and geochemistry of giant quartz veins from the Bundelkhand Craton, central India and their implications. J Earth Syst Sci 116:497–510. https://doi.org/10.1007/s12040-007-0046-y

Plumper O, Putnis A (2009) The Complex Hydrothermal History of Granitic Rocks: Multiple Feldspar Replacement Reactions under Subsolidus Conditions. Journal of Petrology 50:967–987. https://doi.org/10.1093/petrology/egp028

Pradhan VR, Meert JG, Pandit MK, et al (2012) Paleomagnetic and geochronological studies of the mafic dyke swarms of Bundelkhand craton, central India: Implications for the tectonic evolution and paleogeographic reconstructions. Precambrian Research 198–199:51–76. https://doi.org/10.1016/j.precamres.2011.11.011

Putnis A, Hinrichs R, Putnis CV, et al (2007) Hematite in porous red-clouded feldspars: Evidence of large-scale crustal fluid–rock interaction. Lithos 95:10–18. https://doi.org/10.1016/j.lithos.2006.07.004

Que M, Allen AR (1996) Sericitization of plagioclase in the Rosses Granite Complex, Co. Donegal, Ireland. Mineral mag 60:927–936. https://doi.org/10.1180/minmag.1996.060.403.07

Rana SN, Ahirwar SK, Gaur VP, Singh P (2023) Copper–Gold Mineralization and Associated Hydrothermal Alteration around Suwara Area, Southern Part of the Bundelkhand Craton, Central India. Current Science 125:678. https://doi.org/10.18520/cs/v125/i6/678-684

Ray L, Nagaraju P, Singh SP, et al (2016) Radioelemental, petrological and geochemical characterization of the Bundelkhand craton, central India: implication in the Archaean geodynamic evolution. Int J Earth Sci (Geol Rundsch) 105:1087–1107. https://doi.org/10.1007/s00531-015-1229-4

Rout D, Pati JK, Mernagh TP, Panigrahi MK (2025) Fluid Evolution in the Bundelkhand Granite, North Central India: Implications for Hydrothermal Activities in the Bundelkhand Craton. Minerals 15:579. https://doi.org/10.3390/min15060579

Saha L, Pant NC, Pati JK, et al (2011) Neoarchean high-pressure margarite–phengitic muscovite–chlorite corona mantled corundum in quartz-free high-Mg, Al phlogopite–chlorite schists from the Bundelkhand craton, north central India. Contrib Mineral Petrol 161:511–530. https://doi.org/10.1007/s00410-010-0546-7

Sanyal S, Sain A, Rastogi AK, et al (2025) High-K granites from the bundelkhand craton: petrogenesis and geodynamic implication during the NeoArchaean time. ProcIndian Natl Sci Acad. https://doi.org/10.1007/s43538-025-00492-1

Sarkar G, Banerjee S, Maity S, Srivastava HB (2020) Fluid assisted rejuvenation of precursor brittle fractures as the habitats of ductile shear zones: An example from the ~2.6 Ga Bundelkhand Granitoid of north-central India. Journal of Structural Geology 141:104198. https://doi.org/10.1016/j.jsg.2020.104198

Sensarma S, Matin A, Paul D, et al (2018) Reddening of ~2.5 Ga granitoid by high-temperature fluid linked to mafic dyke swarm in the Bundelkhand Craton, north central India. Geological Journal 53:1338–1353. https://doi.org/10.1002/gj.2960

Shankar R, Sreenivas R, Parashuramulu V, Srinivasa Sarma D (2023) Precise Pb-Pb baddeleyite ages and petrogenesis of the NW-SE trending Paleoproterozoic mafic dyke swarm from the Bundelkhand craton, India: Implications to the enriched sub-continental lithospheric mantle. Journal of Asian Earth Sciences 246:105579. https://doi.org/10.1016/j.jseaes.2023.105579

Sibelev OS, Slabunov AI, Mishra S, Singh VK (2021a) Metamorphism of the Central Bundelkhand Greenstone Complex, Indian Shield: Mineral Compositions, Paragenesises, and P–T Path. Petrology 29:404–438. https://doi.org/10.1134/S0869591121040056

Sibelev OS, Slabunov AI, Singh VK, Mishra S (2021b) Metamorphism of the Central Bundelkhand Greenstone Complex of the Bundelkhand Craton, Indian Shield and Its Geodynamic Setting. In: Shandilya AK, Singh VK, Bhatt SC, Dubey CS (eds) Geological and Geo-Environmental Processes on Earth. Springer, Singapore, pp 143–154

Singh PK, Verma SK, Singh VK, et al (2021) Geochronology and petrogenesis of the TTG gneisses and granitoids from the Central Bundelkhand granite-greenstone terrane, Bundelkhand Craton, India: Implications for Archean crustal evolution and cratonization. Precambrian Research 359:106210. https://doi.org/10.1016/j.precamres.2021.106210

Singh VK, Slabunov A (2016) Two Types of Archaean Supracrustal Belts in the Bundelkhand Craton, India: Geology, Geochemistry, Age and Implication for Craton Crustal Evolution. Jour Geol Soc India 88:539–548. https://doi.org/10.1007/s12594-016-0519-1

Slabunov AI, Singh VK (2022) Giant Quartz Veins of the Bundelkhand Craton, Indian Shield: New Geological Data and U-Th-Pb Age. Minerals 12:168. https://doi.org/10.3390/min12020168

Sun S -s., McDonough WF (1989) Chemical and isotopic systematics of oceanic basalts: implications for mantle composition and processes. SP 42:313–345. https://doi.org/10.1144/GSL.SP.1989.042.01.19

Taylor HP (1977) Water/rock interactions and the origin of H_2O in granitic batholiths: Thirtieth William Smith lecture. JGS 133:509–558. https://doi.org/10.1144/gsjgs.133.6.0509

Xie X, Byerly GR, Ferrell Jr. RE (1997) IIb trioctahedral chlorite from the Barberton greenstone belt: crystal structure and rock composition constraints with implications to geothermometry. Contrib Mineral Petrol 126:275–291. https://doi.org/10.1007/s004100050250

Yavuz F, Kumral M, Karakaya N, et al (2015) A Windows program for chlorite calculation and classification. Computers & Geosciences 81:101–113. https://doi.org/10.1016/j.cageo.2015.04.011

Yuguchi T, Sasao E, Ishibashi M, Nishiyama T (2015) Hydrothermal chloritization processes from biotite in the Toki granite, Central Japan: Temporal variations of of the compositions of hydrothermal fluids associated with chloritization. American Mineralogist 100:1134–1152. https://doi.org/10.2138/am-2015-5126

Yuguchi T, Shoubuzawa K, Ogita Y, et al (2019) Role of micropores, mass transfer, and reaction rate in the hydrothermal alteration process of plagioclase in a granitic pluton. American Mineralogist 104:536–556. https://doi.org/10.2138/am-2019-6786

Zang W, Fyfe WS (1995) Chloritization of the hydrothermally altered bedrock at the Igarapé Bahia gold deposit, Carajás, Brazil. Mineral Deposita 30:30–38. https://doi.org/10.1007/BF00208874

Table S1

Sample ID		Al_2O_3	CaO	Fe_2O_3	K_2O	MgO	MnO	Na_2O	P_2O_5	SiO_2	TiO_2	LOI	CIA
		wt%	wt%	wt%	wt%	wt%	wt%	wt%	wt%	wt%	wt%	wt%	%
K-L1-A	**PG**	18.32	1.26	2.54	6.14	0.28	0.05	4.21	0.02	65.47	0.22	1.46	53.6
K-L1-B	**PG**	13.90	0.17	0.61	7.80	0.30	0.01	2.37	0.02	73.00	0.07	1.70	52.4
K-L1-C	**PG**	13.90	0.97	1.31	5.42	0.32	0.03	3.19	0.02	73.00	0.10	1.73	51.9
K-L1-D	**PG**	13.71	0.49	0.91	5.65	0.25	0.01	3.25	0.02	74.01	0.07	1.59	52.6
K-L1-E	**PG**	13.37	0.29	1.03	5.95	0.32	0.03	2.86	b.d.	73.39	0.10	2.61	53.4
K-L1-F	**PG**	14.58	0.64	2.09	5.10	0.48	0.03	3.63	0.05	71.06	0.25	2.07	53.5
K-L1-F1	**PG**	14.49	1.48	2.52	4.95	0.71	0.05	3.81	0.09	70.37	0.28	1.23	50.3
K-L1-G	**PG**	13.64	0.46	0.86	5.38	0.27	0.03	3.64	0.02	74.20	0.08	1.40	51.9
K-L2-A	**GG**	18.30	0.29	3.76	5.74	0.90	0.05	1.54	0.05	63.61	0.62	5.11	66.4
K-L2-B1	**GG**	18.12	0.22	3.40	5.72	0.81	0.05	1.35	0.02	64.73	0.50	5.05	67.3
K-L2-B2	**GG**	20.14	0.24	16.63	4.49	0.80	0.05	0.55	0.07	47.21	1.57	8.23	76.4
K-L2-C	**GG**	17.61	0.13	2.83	5.71	0.83	0.05	1.08	0.02	68.19	0.33	3.20	68.3
K-L2-D	**GG**	16.36	0.25	1.93	5.67	0.46	0.05	2.39	0.02	69.13	0.17	3.56	60.8
K-L2-E	**GG**	20.89	0.11	3.72	6.42	0.86	0.03	1.05	0.02	62.87	0.40	3.59	70.2
K-L3-A	**IG**	13.17	0.22	3.03	3.61	0.80	0.06	1.42	0.02	73.39	0.27	3.99	66.5
K-L3-B	**IG**	15.91	0.27	3.59	5.50	0.80	0.06	1.43	0.02	66.39	0.33	5.65	64.4
K-L3-C	**IG**	15.02	0.25	2.79	5.38	0.70	0.09	1.91	0.02	69.00	0.28	4.52	61.5
K-L3-D	**IG**	17.53	0.41	3.80	4.62	0.78	0.08	2.51	0.02	64.45	0.38	5.41	64.0
K-L3-E	**IG**	14.49	0.11	1.40	7.06	0.25	0.05	3.24	0.02	71.91	0.03	1.43	52.4
K-L3-F	**IG**	15.26	0.50	1.39	7.34	0.22	0.05	3.52	0.02	70.18	0.03	1.46	51.0
K-L3-G2	**IG**	17.72	0.66	4.53	4.53	1.19	0.10	3.30	0.02	62.52	0.57	4.85	60.6
K-L3-H2	**IG**	15.83	1.25	4.32	4.84	1.28	0.05	3.53	0.14	64.90	0.43	3.42	54.3
K-L3-I	**IG**	13.85	0.21	1.13	6.85	0.27	0.03	3.37	0.02	73.58	0.03	0.67	50.9
K-L3-J	**IG**	13.73	0.35	1.09	6.33	0.41	0.03	3.36	0.02	73.54	0.15	0.96	51.4

Sample ID		Li	Sc	V	Cr	Co	Ni	Cu	Rb	Sr	Y	Zr	Nb	Ba
		ppm	ppm	ppm	ppm	ppm	ppm	ppm	ppm	ppm	ppm	ppm	ppm	ppm
K-L1-A	**PG**	5.4	4.7	34	11.6	72	8.9	8.5	126	367	9.3	95	7.1	1290
K-L1-B	**PG**	1.7	0.2	8	2.5	93	3.3	1.9	153	156	6.8	65	8.2	1001
K-L1-C	**PG**	2.7	0.4	20	3.1	82	3.8	1.7	104	280	4.8	61	6.4	713
K-L1-D	**PG**	2.6	0.2	13	2.4	98	3.9	1.8	113	212	4.6	48	4.1	772
K-L1-E	**PG**	2.5	0.6	16	4.6	127	4.8	2.6	120	184	5.6	47	7.3	887
K-L1-F	**PG**	4.9	0.8	30	7.5	92	4.1	2.9	91	224	13.5	59	6.6	731
K-L1-F1	**PG**	6.6	4.3	39	11.7	99	8.0	2.4	90	317	13.4	147	6.9	770
K-L1-G	**PG**	4.6	0.9	12	3.0	123	4.3	1.6	106	268	3.9	59	2.7	1040
K-L2-A	**GG**	9.4	6.0	56	21.9	43	13.4	14.1	124	68	34.2	376	23.6	825
K-L2-B1	**GG**	7.8	5.2	50	18.4	67	12.1	12.4	126	55	30.5	326	20.3	804
K-L2-B2	**GG**	4.7	3.1	26	8.0	85	8.8	35.4	125	117	19.4	173	26.2	658
K-L2-C	**GG**	12.9	17.2	293	35.2	37	27.3	37.5	111	20	32.5	277	16.9	557
K-L2-D	**GG**	3.4	3.6	32	8.4	46	7.5	7.5	119	21	22.1	259	16.6	676
K-L2-E	**GG**	2.7	5.4	47	5.3	74	4.8	6.8	205	21	37.2	506	26.7	1087

Sample ID		La	Ce	Pr	Nd	Eu	Sm	Tb	Gd	Dy	Ho	Er	Tm	Yb	Lu	Hf	Pb	Th	U
		ppm	ppm	ppm	ppm	ppm	ppm	ppm	ppm	ppm	ppm	ppm	ppm	ppm	ppm	ppm	ppm	ppm	ppm
K-L1-A	**PG**	21.6	33.5	5.28	18.19	1.00	3.76	0.37	2.43	2.05	0.36	1.03	0.16	1.14	0.17	2.95	29.2	14.8	2.11
K-L1-B	**PG**	3.7	22.0	0.86	3.18	0.43	1.25	0.20	1.06	1.28	0.27	0.83	0.14	1.00	0.15	2.58	35.4	21.6	4.41
K-L1-C	**PG**	8.9	21.4	1.65	5.38	0.40	1.15	0.14	0.83	0.86	0.17	0.56	0.10	0.70	0.11	2.43	36.4	17.6	3.04
K-L1-D	**PG**	13.1	51.7	2.33	7.09	0.44	1.32	0.14	0.87	0.82	0.16	0.50	0.09	0.59	0.09	1.95	32.3	17.6	2.73
K-L1-E	**PG**	9.5	98.1	2.12	7.09	0.50	1.59	0.18	1.04	0.97	0.19	0.59	0.11	0.76	0.11	1.78	42.5	14.8	2.41
K-L1-F	**PG**	48.5	87.2	7.69	24.14	0.95	3.74	0.42	2.99	2.32	0.42	1.28	0.20	1.26	0.17	1.80	38.2	16.9	3.29
K-L1-F1	**PG**	42.2	90.0	8.91	29.88	1.10	4.80	0.51	3.48	2.75	0.48	1.44	0.22	1.57	0.23	4.17	32.5	21.5	3.28
K-L1-G	**PG**	17.3	37.3	2.93	8.92	0.57	1.65	0.14	0.96	0.77	0.14	0.41	0.07	0.47	0.08	1.89	33.7	13.0	2.56
K-L2-A	**GG**	136.7	240.9	24.25	78.79	1.72	11.75	1.27	9.12	6.51	1.14	3.46	0.50	3.33	0.49	10.31	22.1	79.3	6.53
K-L2-B1	**GG**	126.2	228.7	22.98	73.96	1.54	11.36	1.17	8.27	6.06	1.06	3.16	0.45	3.00	0.45	9.16	21.0	73.6	6.20
K-L2-B2	**GG**	50.7	112.2	9.64	30.72	0.78	5.30	0.67	4.23	3.93	0.73	2.22	0.35	2.39	0.36	5.67	33.9	46.7	7.33
K-L2-C	**GG**	80.0	150.2	15.60	51.26	1.44	8.64	1.05	6.77	5.96	1.15	3.27	0.51	3.31	0.49	6.89	84.3	39.5	5.02
K-L2-D	**GG**	109.9	196.8	18.32	57.42	1.06	7.66	0.77	5.63	4.11	0.70	2.19	0.32	2.18	0.32	7.05	14.2	62.8	5.39
K-L2-E	**GG**	193.4	343.9	32.65	103.85	1.90	15.04	1.50	10.46	7.61	1.30	3.81	0.56	3.73	0.56	12.96	13.2	74.1	6.71

b.d. Below Detection
PG: Pink Granitoids
GG: Grey Granitoids
IG: Intermediate Granitoids

Table S2

Grey Granitoids

Plagioclase

Spots	SiO2	Al2O3	Na2O	Formula	Ab%
1	77.7	13.4	9	(Na0.74)(Si3.31Al0.67)O8	100
2	67	19.7	13.2	(Na1.13)(Si2.95Al1.02)O8	100
3	66.5	20.4	13.1	(Na1.12)(Si2.93Al1.06)O8	100
4	66.7	21.2	12	(Na1.02)(Si2.92Al1.10)O8	100
5	67	20.4	12.8	(Na1.09)(Si2.94Al1.05)O8	100
6	65.9	20.6	13.3	(Na0.79)(Si3.05Al1.01)O8	100
7	65.9	20.6	13.6	(Na0.77)(Si3.07Al0.99)O8	100
8	66.7	19.7	13.6	(Na0.77)(Si3.06Al1.00)O8	100
9	71.5	19.3	9	(Na0.75)(Si3.08Al0.98)O8	100
10	71	19.7	9.3	(Na0.78)(Si3.06Al1.00)O8	100
11	70.2	20.4	9.4	(Na0.79)(Si3.03Al1.04)O8	100
12	71	19.5	9.6	(Na0.80)(Si3.06Al0.99)O8	100
13	70.4	20.4	9	(Na0.75)(Si3.03Al1.04)O8	100
14	70.8	19.8	9.4	(Na1.14)(Si2.91Al1.07)O8	100
15	70.8	19.7	9.6	(Na0.80)(Si3.05Al1.00)O8	100
16	70	20.4	9.7	(Na0.81)(Si3.02Al1.04)O8	100
17	70.8	20.2	9	(Na0.75)(Si3.04Al1.02)O8	100
18	70.8	19.8	9.4	(Na0.79)(Si3.05Al1.01)O8	100
19	71.2	19.5	9.2	(Na1.16)(Si2.91Al1.07)O8	100
20	71.2	19.1	9.7	(Na0.81)(Si3.07Al0.97)O8	100
21	71.2	19.7	9.2	(Na1.16)(Si2.94Al1.02)O8	100
22	71.2	19.7	9.2	(Na0.77)(Si3.06Al1.00)O8	100
23	71.5	19.1	9.4	(Na0.78)(Si3.08Al0.97)O8	100
24	71	19.3	9.6	(Na0.80)(Si3.06Al0.98)O8	100

Epidote

Spt	CaO	FeO	SiO2	Al2O3	MgO	Fe/(Fe+Al)	Formula
1	25.9	18	34	20.8	0	38.043	Ca2.35(Al2.08Fe^{3+}1.27)Si2.88O$_{12}$(OH)
2	27.6	20.7	34.4	17.4	0	45.773	Ca2.52(Al1.75Fe^{3+}1.48)Si2.94O$_{12}$(OH)
3	28.4	15.2	35.1	21.2	0	33.719	Ca2.52(Al2.07Fe^{3+}1.05)Si2.91O$_{12}$(OH)
4	26.2	17	35.5	19.7	1.7	37.976	Ca2.33(Al1.93Fe^{3+}1.18Mg0.21)Si2.95O$_{12}$(OH)
5	26.4	15.7	36.4	21.5	0	34.129	Ca2.32(Al2.08Fe^{3+}1.08)Si2.99O$_{12}$(OH)
6	24.8	12.2	39.8	21.9	0	28.329	Ca2.14(Al2.08Fe^{3+}0.82)Si3.21O$_{12}$(OH)
7	24.6	15.3	38.5	21.4	0	33.655	Ca2.14(Al2.05Fe^{3+}1.04)Si3.13O$_{12}$(OH)
8	27.8	13.1	36.2	22.9	0	28.871	Ca2.42(Al2.20Fe^{3+}0.89)Si2.95O$_{12}$(OH)
9	24.1	11.2	40	24.6	0	24.416	Ca2.03(Al2.28Fe^{3+}0.74)Si3.15O$_{12}$(OH)
10	23.2	12.1	40.2	24.6	0	25.871	Ca1.96(Al2.28Fe^{3+}0.80)Si3.16O$_{12}$(OH)
11	14.7	14.7	50.5	20	0	34.276	Ca1.20(Al1.79Fe^{3+}0.93)Si3.84O$_{12}$(OH)
12	21.4	14.2	41.3	23.1	0	30.37	Ca1.81(Al2.15Fe^{3+}0.94)Si3.26O$_{12}$(OH)
13	21.3	10.7	43.2	24.9	0	23.366	Ca1.76(Al2.26Fe^{3+}0.69)Si3.33O$_{12}$(OH)
14	20.6	8	44.7	26.8	0	17.478	Ca1.67(Al2.38Fe^{3+}0.51)Si3.38O$_{12}$(OH)
15	16.8	8.4	43.9	27.8	3.3	17.654	Ca1.35(Al2.45Fe^{3+}0.53Mg0.37)Si3.29O$_{12}$(OH)
16	23.1	11.6	40.2	24.9	0	24.843	Ca1.95(Al2.31Fe^{3+}0.76)Si3.16O$_{12}$(OH)
17	22.8	12	40.2	24.9	0	25.481	Ca1.92(Al2.31Fe^{3+}0.79)Si3.16O$_{12}$(OH)
18	19.3	14	43.9	22.7	0	30.44	Ca1.61(Al2.09Fe^{3+}0.91)Si3.42O$_{12}$(OH)
19	23.5	12.4	40.2	23.8	0	26.99	Ca1.99(Al2.22Fe^{3+}0.82)Si3.18O$_{12}$(OH)
20	24.2	12	38.1	25.7	0	24.885	Ca2.06(Al2.40Fe^{3+}0.80)Si3.02O$_{12}$(OH)
21	21.8	12.9	40.6	24.6	0	27.118	Ca1.84(Al2.28Fe^{3+}0.85)Si3.20O$_{12}$(OH)
22	12.6	9.8	55.6	22.1	0	23.933	Ca0.98(Al1.89Fe^{3+}0.60)Si4.04O$_{12}$(OH)
23	13.2	8.2	53.7	24.9	0	18.941	Ca1.03(Al2.13Fe^{3+}0.50)Si3.89O$_{12}$(OH)
24	11.1	11.1	58	19.8	0	28.457	Ca0.86(Al1.69Fe^{3+}0.67)Si4.21O$_{12}$(OH)
25	16.5	11.6	41.9	24.8	5.1	24.918	Ca1.36(Al2.25Fe^{3+}0.75Mg0.58)Si3.22O$_{12}$(OH)

Pink Granitoids

Plagioclase

SPT	SiO2	Al2O3	Na2O	CaO	K2O	Ab%	An%	Or%	Plagioclase	Mineral_ID	Formula
1	66.4	22.6	7.5	3.5	0	79.5	20.5	0.0	Oligoclase	Plagioclase	(Na0.63Ca0.16)(Si2.89Al1.16)O8
2	70.2	20.4	8.1	1.2	0	92.4	7.6	0.0	Albite	Plagioclase	(Na0.68Ca0.06)(Si3.03Al1.04)O8
3	66.5	22.2	7.4	3.9	0	77.4	22.6	0.0	Oligoclase	Plagioclase	(Na0.63Ca0.18)(Si2.90Al1.14)O8
4	64.6	23.3	6.9	5.1	0	71.0	29.0	0.0	Oligoclase	Plagioclase	(Na0.59Ca0.24)(Si2.83Al1.20)O8
5	65.7	22.9	6.7	4.7	0	72.1	27.9	0.0	Oligoclase	Plagioclase	(Na0.57Ca0.22)(Si2.87Al1.18)O8
6	65.8	23.2	6.7	4.3	0	73.8	26.2	0.0	Oligoclase	Plagioclase	(Na0.57Ca0.20)(Si2.87Al1.19)O8
7	70.2	20.3	8	1.5	0	90.6	9.4	0.0	Albite	Plagioclase	(Na0.67Ca0.07)(Si3.03Al1.03)O8
8	64.3	23.8	7.5	4.4	0	75.5	24.5	0.0	Oligoclase	Plagioclase	(Na0.64Ca0.21)(Si2.82Al1.23)O8
9	64.7	23.4	7	4.8	0	72.5	27.5	0.0	Oligoclase	Plagioclase	(Na0.59Ca0.23)(Si2.83Al1.21)O8
10	64.5	23.4	7.2	4.9	0	72.7	27.3	0.0	Oligoclase	Plagioclase	(Na0.61Ca0.23)(Si2.83Al1.21)O8
11	65.9	22.8	7.3	4	0	76.8	23.2	0.0	Oligoclase	Plagioclase	(Na0.62Ca0.19)(Si2.87Al1.17)O8
12	65.5	22.5	7.1	4.1	0	75.8	24.2	0.0	Oligoclase	Plagioclase	(Na0.60Ca0.19)(Si2.88Al1.17)O8
13	65.6	23.3	6.9	4.1	0	75.3	24.7	0.0	Oligoclase	Plagioclase	(Na0.58Ca0.19)(Si2.86Al1.20)O8
14	66	22.5	7	4.5	0	73.8	26.2	0.0	Oligoclase	Plagioclase	(Na0.59Ca0.21)(Si2.88Al1.16)O8
15	66.3	22.3	7.2	4.3	0	75.2	24.8	0.0	Oligoclase	Plagioclase	(Na0.61Ca0.20)(Si2.89Al1.15)O8
16	65.1	23.6	6.9	4.4	0	73.9	26.1	0.0	Oligoclase	Plagioclase	(Na0.58Ca0.21)(Si2.84Al1.21)O8
17	66.5	21.9	7.4	4.1	0	76.6	23.4	0.0	Oligoclase	Plagioclase	(Na0.63Ca0.19)(Si2.90Al1.13)O8
18	75	16.5	6	2.6	0	80.7	19.3	0.0	Oligoclase	Plagioclase	(Na0.50Ca0.12)(Si3.20Al0.83)O8
19	65	23	7.2	4.8	0	73.1	26.9	0.0	Oligoclase	Plagioclase	(Na0.61Ca0.23)(Si2.84Al1.19)O8
20	65.9	23.6	7.3	3.2	0	80.5	19.5	0.0	Oligoclase	Plagioclase	(Na0.62Ca0.15)(Si2.86Al1.21)O8
24	66.4	23.3	7	1.2	2	78.0	7.4	14.7	Albite	Plagioclase	(Na0.59Ca0.06K0.11)(Si2.90Al1.20)O8
25	65.6	23.7	7.2	1	2.5	76.6	5.9	17.5	Albite	Plagioclase	(Na0.61Ca0.05K0.14)(Si2.87Al1.22)O8
26	67.9	21.7	7.6	2	0.9	81.7	11.9	6.4	Oligoclase	Plagioclase	(Na0.64Ca0.09K0.05)(Si2.95Al1.11)O8
27	66.7	23.4	7.1	1	1.9	79.8	6.2	14.0	Albite	Plagioclase	(Na0.60Ca0.05K0.11)(Si2.90Al1.20)O8
28	67.5	22.5	7.5	1.5	1	83.5	9.2	7.3	Albite	Plagioclase	(Na0.63Ca0.07K0.06)(Si2.93Al1.15)O8
29	65	23.1	6.7	4.3	0.8	69.8	24.7	5.5	Oligoclase	Plagioclase	(Na0.57Ca0.20K0.04)(Si2.85Al1.19)O8
30	67.7	22.7	7.1	0.7	1.8	81.9	4.5	13.7	Albite	Plagioclase	(Na0.60Ca0.03K0.10)(Si2.94Al1.16)O8
31	66.1	23.9	7.5	0	2.5	82.0	0.0	18.0	Albite	Plagioclase	(Na0.63K0.14)(Si2.88Al1.23)O8
32	66.5	22.6	7.9	1	1.9	81.4	5.7	12.9	Albite	Plagioclase	(Na0.67Ca0.05K0.11)(Si2.91Al1.17)O8
33	68.2	21.4	7.7	1.9	0.7	83.6	11.4	5.0	Oligoclase	Plagioclase	(Na0.65Ca0.09K0.04)(Si2.96Al1.10)O8
34	67.2	22.7	7.3	1.5	1.4	80.7	9.2	10.2	Albite	Plagioclase	(Na0.61Ca0.07K0.08)(Si2.92Al1.16)O8
35	71.6	19.8	8.6	0	0	100.0	0.0	0.0	Albite	Albite	(Na0.72)(Si3.07Al1.00)O8
36	71.1	20.5	8.4	0	0	100.0	0.0	0.0	Albite	Albite	(Na0.70)(Si3.05Al1.04)O8
37	71.4	20	8.6	0	0	100.0	0.0	0.0	Albite	Albite	(Na0.72)(Si3.06Al1.01)O8
38	70.9	20.5	8.7	0	0	100.0	0.0	0.0	Albite	Albite	(Na0.72)(Si3.04Al1.04)O8
39	71.4	20.1	8.6	0	0	100.0	0.0	0.0	Albite	Albite	(Na0.71)(Si3.06Al1.02)O8
40	70.6	21.3	8.1	0	0	100.0	0.0	0.0	Albite	Albite	(Na0.67)(Si3.03Al1.08)O8

Epidote

spt	CaO	SiO2	Al2O3	FeO	MgO	MnO	Fe/(Fe+Al)	Formula
1	26.748	35.543	19.487	17.392	0.83	0	0.388	Ca2.39(Al1.91Fe^{3+}1.21Mg0.10)Si2.96O$_{12}$(OH)
2	27.245	35.889	22.084	14.781	0	0	0.322	Ca2.39(Al2.14Fe^{3+}1.01)Si2.94O$_{12}$(OH)
3	27.399	37.404	22.851	12.346	0	0	0.277	Ca2.37(Al2.17Fe^{3+}0.83)Si3.02O$_{12}$(OH)
4	28.92	35.459	23.026	12.595	0	0	0.28	Ca2.53(Al2.22Fe^{3+}0.86)Si2.89O$_{12}$(OH)
5	28.401	36.365	22.492	12.742	0	0	0.287	Ca2.48(Al2.16Fe^{3+}0.87)Si2.96O$_{12}$(OH)
6	22.707	39.433	20.451	17.408	0	0	0.377	Ca1.98(Al1.96Fe^{3+}1.18)Si3.20O$_{12}$(OH)
7	29.066	35.039	22.654	13.241	0	0	0.293	Ca2.56(Al2.19Fe^{3+}0.91)Si2.88O$_{12}$(OH)
8	27.589	35.544	23.082	13.785	0	0	0.298	Ca2.42(Al2.22Fe^{3+}0.94)Si2.90O$_{12}$(OH)
9	27.422	37.007	24.76	10.811	0	0	0.237	Ca2.35(Al2.34Fe^{3+}0.72)Si2.96O$_{12}$(OH)
10	27.964	36.128	23.045	12.863	0	0	0.284	Ca2.44(Al2.21Fe^{3+}0.87)Si2.94O$_{12}$(OH)
11	27.573	36.165	23.257	13.005	0	0	0.284	Ca2.40(Al2.23Fe^{3+}0.88)Si2.94O$_{12}$(OH)
12	27.299	36.173	23.263	13.265	0	0	0.288	Ca2.38(Al2.23Fe^{3+}0.90)Si2.94O$_{12}$(OH)
13	24.762	36.576	24.758	12.226	0	1.678	0.259	Ca2.14Mn0.11(Al2.35Fe^{3+}0.82)Si2.95O$_{12}$(OH)
14	27.673	35.687	24.168	12.472	0	0	0.268	Ca2.40(Al2.31Fe^{3+}0.85)Si2.89O$_{12}$(OH)
15	26.583	36.365	21.736	15.316	0	0	0.333	Ca2.34(Al2.10Fe^{3+}1.05)Si2.98O$_{12}$(OH)
16	27.589	35.116	21.19	16.104	0	0	0.35	Ca2.45(Al2.07Fe^{3+}1.12)Si2.91O$_{12}$(OH)
17	27.674	36.532	24.107	11.686	0	0	0.256	Ca2.39(Al2.29Fe^{3+}0.79)Si2.94O$_{12}$(OH)
18	27.198	37.59	25.741	9.471	0	0	0.207	Ca2.31(Al2.40Fe^{3+}0.63)Si2.98O$_{12}$(OH)
19	27.403	36.126	23.61	12.862	0	0	0.279	Ca2.38(Al2.26Fe^{3+}0.87)Si2.93O$_{12}$(OH)
20	27.534	37.61	23.413	11.443	0	0	0.257	Ca2.37(Al2.22Fe^{3+}0.77)Si3.02O$_{12}$(OH)

Sericite

spt	SiO2	Al2O3	K2O	FeO	MgO	Na2O	Formula
1	47.063	32.12	13.492	5.918	1.492	0	(K1.14)(Al1.60Fe0.33Mg0.15)(Si3.11Al0.89)O$_{10}$(OH)$_2$
2	46.421	33.443	14.095	6.047	0	0	(K1.19)(Al1.69Fe0.34)(Si3.08Al0.92)O$_{10}$(OH)$_2$
3	48.774	32.876	12.408	3.731	1.161	0.944	(K1.03Na0.12)(Al1.68Fe0.20Mg0.11)(Si3.17Al0.83)O$_{10}$(OH)$_2$
4	47.919	33.443	13.492	3.474	1.658	0	(K1.12)(Al1.69Fe0.19Mg0.16)(Si3.12Al0.88)O$_{10}$(OH)$_2$
5	45.565	39.3	13.974	1.158	0	0	(K1.15)(Al1.93Fe0.06)(Si2.94Al1.06)O$_{10}$(OH)$_2$
6	48.56	34.198	13.372	2.831	1.161	0	(K1.10)(Al1.74Fe0.15Mg0.11)(Si3.14Al0.86)O$_{10}$(OH)$_2$
7	48.346	33.254	13.251	3.731	1.492	0	(K1.10)(Al1.69Fe0.20Mg0.14)(Si3.14Al0.86)O$_{10}$(OH)$_2$
8	48.56	34.954	12.769	2.831	1.326	0	(K1.05)(Al1.76Fe0.15Mg0.13)(Si3.12Al0.88)O$_{10}$(OH)$_2$
9	38.292	24.751	10.722	3.345	1.658	0.809	(K1.13Na0.13)(Al1.57Fe0.23Mg0.20)(Si3.16Al0.84)O$_{10}$(OH)$_2$
10	46.421	36.843	12.89	2.573	1.161	0	(K1.06)(Al1.81Fe0.14Mg0.11)(Si3.00Al1.00)O$_{10}$(OH)$_2$
11	47.705	37.599	0	1.93	0	0.944	(Na0.12)(Al2.16Fe0.11)(Si3.19Al0.81)O$_{10}$(OH)$_2$
12	51.555	33.443	14.938	0	0	0	(K1.22)(Al1.83)(Si3.30Al0.70)O$_{10}$(OH)$_2$
13	45.993	38.544	13.854	1.801	0	0	(K1.14)(Al1.90Fe0.10)(Si2.97Al1.03)O$_{10}$(OH)$_2$
14	46.635	24.751	11.565	0	0	0	(K1.12)(Al1.77)(Si3.55Al0.45)O$_{10}$(OH)$_2$
15	53.053	34.576	7.71	1.544	0	3.1	(K0.61Na0.37)(Al1.85Fe0.08)(Si3.31Al0.69)O$_{10}$(OH)$_2$
16	53.267	34.954	9.276	0	0	2.561	(K0.74Na0.31)(Al1.88)(Si3.32Al0.68)O$_{10}$(OH)$_2$
17	51.127	37.599	11.203	0	0	0	(K0.89)(Al1.97)(Si3.20Al0.80)O$_{10}$(OH)$_2$

Mineral	Oxygen Basis
Feldspar	8 O
Epidote	12.5 O
Mica	11 O

Table S3

Grey Granitoids

Spt No	(%)[SiO2	Al2O3	FeO	MnO	MgO	Al(IV)	[Octahedral vacant]	Fe/(Fe+Mg)	R2+	%[Al-chl	Fe-chl	Mg-chl]	[TCN85-AlIV(oC) (#1)	TKML87-AlIV(oC)(#2)	TC88-AlIV(oC) (#3)	TJ91-AlIV(oC) (#4)	TZF95-AlIV(oC) (#5)	TX97-AlIV(oC) (#6)	Average(oC)
S1	37.9	17.6	18.4	0	26.2	0.7123	0.1868	0.2826	4.7272	15.4671	26.1942	58.3387	165	190	167	167	174	179	174
S2	38.1	17.6	19.7	0	24.7	0.6789	0.2243	0.3089	4.6482	15.6374	28.7414	55.6212	157	185	157	157	165	157	163
S3	30.8	20.4	29.8	0	19.1	1.1541	0	0.4675	4.8459	18.7864	36.8028	44.4109	258	297	310	314	251	242	279
S4	31.9	18.7	25.7	0	22.1	1.0573	0	0.3956	4.9427	17.1885	31.546	51.2656	238	271	278	281	237	242	258
S5	32.5	20.4	25.7	0	21.4	1.0538	0.0357	0.4029	4.839	18.2684	33.2878	48.4438	237	271	277	280	235	238	256
S6	32.9	19.1	26	0	21.9	1.0049	0.0175	0.3998	4.9425	17.0905	33.321	49.5885	227	261	262	264	225	223	244
S7	31.8	23.4	21.9	0.6	22.3	1.165	0.0644	0.3552	4.6419	20.8706	28.8132	50.3162	261	291	313	314	264	294	290
S8	33.6	21.4	20.8	0.5	23.7	1.0262	0.0899	0.3299	4.704	19.0056	27.7469	53.2475	231	260	268	269	236	260	254
S9	35	22	17	0.6	25.4	0.9656	0.1583	0.273	4.5594	19.3865	23.9905	56.623	218	243	249	248	229	265	242
S10	33	22.3	20.1	0.4	24.1	1.0852	0.0756	0.3187	4.6881	19.6918	26.4711	53.8371	244	272	287	287	250	284	271
S11	34	21.1	20.2	0.7	24.1	1.0009	0.0959	0.3198	4.7115	18.7424	27.102	54.1556	226	254	260	260	232	256	248
S12	33	21.6	21	0.8	23.5	1.0659	0.0658	0.3339	4.7366	19.267	27.7042	53.0287	240	269	281	282	244	271	265
S13	31.9	22.4	23	0.8	22	1.1392	0.0446	0.3697	4.727	20.0825	30.0204	49.8971	255	287	305	306	257	279	282
S14	32.9	22.8	20.8	0.6	22.9	1.0875	0.1018	0.3375	4.6069	20.3204	28.048	51.6316	244	274	288	289	249	276	270
S15	33.7	23.3	21.1	0.6	21.3	1.0233	0.1895	0.3572	4.4083	21.0348	30.3194	48.6458	231	261	268	269	233	247	252
S16	33.4	22	20.3	0	24.3	1.0572	0.0851	0.3191	4.6876	19.3116	26.7269	53.9615	238	266	278	278	244	275	263
S17	33.2	21.3	21.8	0	23.7	1.0511	0.0638	0.3404	4.7575	18.7811	28.3536	52.8654	236	266	276	277	241	264	260
S18	35.9	21.3	19.5	0	23.4	0.8714	0.2225	0.3186	4.4612	18.933	28.4487	52.6184	198	226	219	219	205	215	214
S19	32.8	21.8	21.5	0	24	1.0918	0.0472	0.3345	4.7665	19.1344	27.5746	53.2909	245	274	290	290	250	279	271
S20	33.9	20.6	20.6	0.6	24.2	0.9968	0.0787	0.3232	4.7673	18.301	27.3105	54.3884	225	253	259	259	231	253	247
S21	33.3	20.4	21.4	0.5	24.3	1.0345	0.036	0.3307	4.8574	18.0643	27.5003	54.4353	233	262	271	272	238	262	256
S22	33.7	20.9	20.7	0.7	24.2	1.0201	0.0689	0.3243	4.7732	18.5251	27.2107	54.2642	230	258	267	267	236	260	253
S23	33	20.9	22	0.9	23.3	1.0544	0.045	0.3463	4.8108	18.6741	28.6598	52.6661	237	267	278	278	241	262	261
S24	34.2	20	22.1	0	23.7	0.9614	0.0858	0.3434	4.7813	17.7057	29.2163	53.078	217	247	248	249	221	233	236
S25	34.4	21.1	21.9	0	22.5	0.9511	0.1509	0.3532	4.5961	18.8411	30.3326	50.8263	215	246	244	246	218	226	233
S26	32.8	21.8	23	0	22.4	1.0708	0.0764	0.3655	4.6999	19.3674	30.2887	50.3439	241	272	283	284	243	259	264
S27	32	21.9	22.2	0	24	1.1476	0.0028	0.3416	4.8441	19.1815	27.6406	53.178	257	287	308	308	261	294	286
S28	32.6	23.2	21.6	0	22.7	1.1136	0.0969	0.348	4.5957	20.506	28.7363	50.7577	250	280	297	297	253	280	276
S29	32.8	22.2	22.4	0	22.6	1.0802	0.0844	0.3573	4.6667	19.686	29.6153	50.6986	243	274	286	287	245	266	267
S30	33.2	21.8	22.1	0	22.9	1.05	0.0915	0.3512	4.6756	19.319	29.342	51.339	236	267	276	277	239	259	259
S31	32	20.7	23.2	0.8	23.3	1.1226	0	0.3584	4.8774	18.6299	28.3211	53.0491	252	283	300	301	254	279	278
S32	33.2	21.6	21.4	0	23.8	1.0575	0.0706	0.3353	4.7307	19.0258	27.941	53.0332	238	267	279	279	243	268	262
S33	33.5	21.9	20.2	0	24.4	1.05	0.0864	0.3171	4.6907	19.2174	26.617	54.1656	236	264	276	276	243	273	261
S34	33	22.6	20.8	0.6	23	1.0786	0.1004	0.3366	4.6203	20.1377	28.0168	51.8456	242	272	285	286	247	274	268
S35	33.6	21.6	21.2	0	23.2	1.0171	0.1129	0.3389	4.6443	19.1942	28.652	52.1538	229	259	266	266	234	253	251
S36	34.5	20.8	18.7	0	25.9	0.9816	0.0907	0.2883	4.7462	18.1471	24.6886	57.1644	222	247	254	253	231	263	245
S37	32.9	21.8	20.9	0	24.4	1.0884	0.0486	0.3246	4.766	19.103	26.8068	54.0902	244	273	288	289	250	282	271
S38	33.5	20.3	20	0.9	25.3	1.0334	0.026	0.3072	4.8887	17.9353	25.5168	56.5479	233	260	271	270	240	272	258
S39	32.6	22.8	20	0	24.5	1.1252	0.0597	0.3141	4.6958	19.9456	25.8343	54.2201	252	280	300	300	259	299	282
S40	34.8	20.3	19.2	0	35.6	1.2781	0	0.2323	4.7219	17.6037	4.2981	78.0982	285	306	350	346	299	383	328
S41	34.9	20.8	18.4	0	25.8	0.9543	0.1154	0.2858	4.6995	18.1778	24.7821	57.0401	216	242	245	245	225	256	238
S42	34.8	21.8	19.6	0	23.7	0.9524	0.1727	0.3169	4.5296	19.3062	27.5967	53.0972	215	243	245	245	222	242	235
S43	32.3	22.4	22.7	0	22.6	1.1174	0.0606	0.3604	4.7009	19.8336	29.5436	50.6228	251	282	298	299	253	276	277
S44	33.3	21.6	19.7	0.6	24.8	1.0631	0.0595	0.3083	4.7585	19.0408	25.6538	55.3053	239	266	280	280	246	281	265
S45	33.9	20.8	19.4	0.6	25.3	1.0155	0.0636	0.3008	4.7936	18.316	25.324	56.36	229	256	265	265	237	269	254
S46	33.3	21.7	20.7	0.5	23.8	1.0527	0.0791	0.3279	4.71	19.2372	27.3874	53.3755	237	265	277	277	242	269	261
S47	34.5	21.3	18.6	0	25.9	0.9967	0.096	0.2872	4.7153	18.5074	24.5617	56.9309	225	251	259	258	234	269	249
S48	33.5	21.1	19.5	0.6	25.2	1.0445	0.0525	0.3027	4.798	18.5847	25.2645	56.1508	235	262	274	274	243	278	261
S49	33.6	21.5	19.4	0.7	24.8	1.0414	0.0741	0.305	4.7361	18.9931	25.5837	55.4232	234	261	273	273	242	276	260
S50	34.1	20.9	19.5	0.6	24.9	0.9991	0.0848	0.3052	4.7466	18.4629	25.8909	55.6462	225	252	260	259	233	262	249
S51	33.4	21.2	20.1	0.6	24.7	1.0483	0.0557	0.3134	4.7845	18.7146	26.1255	55.16	236	263	276	275	243	274	261
S52	34.4	20.5	18.2	0.5	26.3	0.988	0.0698	0.2796	4.8027	17.9487	23.7982	58.253	223	248	256	255	233	269	247
S53	33.4	22.1	20	0	24.6	1.0641	0.0807	0.3132	4.6938	19.3396	26.2011	54.4593	239	267	281	280	246	279	265

Pink Granitoids

	(%)[SiO2	Al2O3	FeO	MnO	MgO	Al(IV)	[Octahedral vacant]	Fe/(Fe+Mg)	R2+	%[Al-chl	Fe-chl	Mg-chl]	[TCN85-AlIV(oC) (#1)	TKML87-AlIV(oC)(#2)	TC88-AlIV(oC) (#3)	TJ91-AlIV(oC) (#4)	TZF95-AlIV(oC) (#5)	TX97-AlIV(oC) (#6)	Average(oC)
S1	34.1	19.5	27.2	0	19.2	0.9009	0.1435	0.4428	4.6687	17.8323	37.7499	44.4178	205	242	228	233	199	171	213
S2	34.3	18.4	27.3	0	20.1	0.8803	0.1059	0.4324	4.8019	16.7321	37.0284	46.2394	200	237	221	226	196	169	208
S3	33.8	19.1	27.7	0	19.4	0.9163	0.1106	0.4447	4.752	17.4358	37.7628	44.8015	208	245	233	237	202	175	217
S4	32.9	19.2	28.5	0	19.3	0.9767	0.063	0.4531	4.8342	17.5127	37.9534	44.5339	221	259	253	257	214	191	233
S5	33.8	19.4	29	0	17.8	0.9008	0.1474	0.4775	4.6569	17.9108	40.5157	41.5735	205	244	228	234	196	156	211
S6	35.1	18.5	26.4	0	19.9	0.8225	0.1644	0.4267	4.6843	16.9119	37.067	46.0211	188	224	203	207	184	153	193
S7	33.7	18.5	28.3	0	19.5	0.9132	0.0854	0.4488	4.8306	16.8833	38.0968	45.0199	207	245	232	237	201	173	216
S8	34.6	19.3	26.7	0	18.9	0.8509	0.1842	0.4421	4.5966	17.7982	38.1096	44.0923	194	231	212	217	189	155	200
S9	34.9	19.1	26.3	0	19.7	0.8463	0.1708	0.4282	4.6413	17.448	37.0257	45.5263	193	229	211	215	189	160	200
S10	35.5	18.7	25.5	0	18.3	0.7445	0.266	0.4387	4.4574	17.6238	38.7455	43.6307	171	208	178	182	166	123	171
S11	35.2	18.7	27.4	0	18.7	0.8052	0.195	0.4511	4.6099	17.2291	39.1849	43.586	184	222	197	202	178	137	187
S12	35.7	18.9	25.1	0	20.3	0.7975	0.2016	0.4096	4.5977	17.2305	35.9511	46.8184	183	217	195	198	180	152	188
S13	34.4	19.4	28	0	18.1	0.8624	0.1803	0.4646	4.5968	17.9166	39.7954	42.2879	196	235	216	221	189	150	201
S14	34.5	18.6	26.7	0	20.2	0.8702	0.1241	0.4258	4.7575	16.9222	36.5857	46.4921	198	234	218	222	194	169	206
S15	34.9	18.4	27.3	0	19.4	0.8289	0.1563	0.4412	4.7022	16.8592	38.1729	44.9679	189	226	205	209	184	149	194
S16	32.4	18.9	27.8	0	21	1.0338	0	0.4262	4.9662	17.0744	34.9316	47.994	233	269	271	274	229	221	250
S17	33.2	19.5	26.5	0	20.8	0.9827	0.0617	0.4168	4.8323	17.5867	34.9567	47.4566	222	257	254	258	219	209	237
S18	33.4	19.1	27	0	20.4	0.9549	0.0713	0.4261	4.8313	17.3083	35.9252	46.7665	216	252	246	249	212	196	229
S19	35.3	18.8	26	0	20	0.8197	0.1784	0.4217	4.6451	17.1448	36.714	46.1412	187	223	202	206	184	154	193
S20	34.1	18.2	27.5	0	20.2	0.8896	0.0886	0.433	4.8445	16.5489	36.9856	46.4655	202	239	225	229	198	172	211
S21	34.7	19.2	27.5	0	18.6	0.8469	0.1812	0.4534	4.6094	17.6689	39.0295	43.3016	193	231	211	216	187	149	198
S22	32.5	17.4	29.1	0	21	1.0087	0	0.4374	4.9913	16.0771	34.8364	49.0865	227	264	263	267	223	208	242
S23	33.1	17.6	27.6	0	21.7	0.9709	0	0.4164	5.0291	15.9345	34.3643	49.7012	219	255	251	254	217	205	234
S24	33.6	18.7	27.3	0	19.8	0.9176	0.0934	0.4361	4.8023	17.1152	37.0402	45.8446	208	245	233	238	203	180	218
S25	35.6	19.3	27.7	0	17.4	0.7725	0.2586	0.4718	4.4518	17.9587	41.0822	40.9591	177	217	187	192	169	118	177
S26	34.1	20.1	28.3	0	17.5	0.8897	0.1907	0.4757	4.5383	18.5972	40.4417	40.9611	202	242	225	230	194	154	208
S27	33.3	19.7	29.4	0	17.6	0.938	0.1295	0.4838	4.6735	18.1839	40.7186	41.0975	212	253	240	246	203	166	220
S28	34	19	27.3	0	19.2	0.8898	0.1345	0.4437	4.7068	17.4618	37.8989	44.6394	202	240	225	229	197	167	210
S29	33.4	19.4	27.7	0	19.5	0.9504	0.0934	0.4435	4.7693	17.6721	37.3909	44.937	215	252	244	248	210	187	226
S30	32.2	20.6	27.5	0	19.8	1.06	0.0484	0.4379	4.7949	18.623	36.0944	45.2826	238	275	279	283	233	225	256
S31	33.8	19.8	27.9	0	18.5	0.9176	0.1465	0.4583	4.6429	18.1782	38.8541	42.9676	208	247	233	238	201	170	216
S32	33.4	19.6	28.2	0	18.1	0.924	0.1397	0.4664	4.6569	18.151	39.4452	42.4038	209	248	236	241	202	169	218
S33	33.7	19.7	26.8	0	19.9	0.9424	0.1108	0.4304	4.7251	17.8848	36.4111	45.7041	213	250	242	245	209	190	225
S34	34.7	19.8	27.3	0	18.2	0.8529	0.2053	0.457	4.5313	18.2614	39.2745	42.4641	194	233	213	218	188	150	199
S35	33.6	20.2	27.7	0	18.6	0.9416	0.142	0.4552	4.6326	18.4963	38.4184	43.0853	213	251	241	246	207	179	223
S36	32.8	20.8	28.2	0	18.2	1.0004	0.1205	0.465	4.638	19.0653	38.7327	42.202	226	265	260	265	218	194	238
S37	32.3	21.3	27.8	0	18.5	1.0461	0.1019	0.4574	4.6484	19.4621	37.7752	42.7627	235	274	275	279	229	212	251
S38	33	20	28.8	0	18.3	0.9749	0.1055	0.4689	4.7087	18.3286	39.2453	42.4261	220	259	252	257	213	184	231
S39	34.5	19.6	27.5	0	18.4	0.8652	0.1842	0.4561	4.582	18.0453	39.0991	42.8556	197	235	217	222	190	154	203
S40	34.8	18.4	27.4	0	19.5	0.8387	0.1463	0.4408	4.7224	16.8269	38.0599	45.1132	191	229	208	213	186	152	197
S41	35	18.4	26.2	0	20.5	0.8387	0.1406	0.4176	4.7394	16.7144	36.176	47.1096	191	227	208	212	188	162	198
S42	34.3	18.5	25.7	0	21.5	0.8989	0.0867	0.4014	4.8409	16.6681	34.3273	49.0046	204	238	227	231	203	188	215
S43	34.3	19.2	25.7	0	20.7	0.8998	0.1228	0.4105	4.7317	17.4	35.1428	47.4572	204	239	228	231	202	185	215
S44	33.3	19.7	26.5	0	20.5	0.9757	0.0787	0.4203	4.7883	17.8058	35.3203	46.8739	220	256	252	256	217	205	234
S45	34.4	18.8	24.6	0	21	0.871	0.1367	0.3966	4.7189	17.1867	34.247	48.5664	198	232	219	221	197	181	208
S46	34.6	18.1	27	0	20.4	0.8584	0.11	0.4261	4.8115	16.4424	36.6763	46.8813	196	232	214	218	192	165	203
S47	33.9	19.5	26.9	0	19.7	0.9209	0.1228	0.4338	4.7107	17.7586	36.8553	45.3861	209	245	235	239	204	182	219
S48	32.9	20.2	27.7	0	19.2	0.9954	0.0917	0.4473	4.7295	18.3994	37.3584	44.2422	225	262	259	263	219	200	238
S49	33	19.9	27.4	0	18.7	0.96	0.1203	0.4511	4.679	18.3735	37.9486	43.6779	217	255	247	252	211	187	228
S50	33.7	19.8	26.8	0	19.8	0.943	0.1154	0.4316	4.7107	17.9865	36.5117	45.5018	213	250	242	246	209	190	225
S51	33.5	20	26.5	0	18.8	0.9255	0.1561	0.4416	4.6061	18.5091	37.4762	44.0146	210	247	236	240	205	180	220
S52	32.8	19.7	27.2	0	20.3	1.0072	0.052	0.4291	4.8368	17.8083	35.7687	46.4231	227	263	262	266	223	211	242
S53	32.7	20.5	26.9	0	19.9	1.0235	0.0761	0.4313	4.7481	18.5625	35.8527	45.5847	231	267	268	271	226	216	247

References

1. Cathelineau M, Nieva D (1985) A chlorite solid solution geothermometer the Los Azufres (Mexico) geothermal system. Contr Mineral and Petrol 91:235–244. https://doi.org/10.1007/BF00413350
2. Kranidiotis P, MacLean WH (1987) Systematics of chlorite alteration at the Phelps Dodge massive sulfide deposit, Matagami, Quebec. Economic Geology 82:1898–1911. https://doi.org/10.2113/gsecongeo.82.7.1898
3. Cathelineau M (1988) Cation site occupancy in chlorites and illites as a function of temperature. Clay Minerals 23:471–485. https://doi.org/10.1180/claymin.1988.023.4.13
4. Jowett EC (1991) Iron and Magnesium into the Hydrothermal Chlorite Geothermometer. In: In Proceedings of the GAC/MAC/SEG Joint Annual Meeting. Toronto, ON, Canada,
5. Zang W, Fyfe WS (1995) Chloritization of the hydrothermally altered bedrock at the Igarapé Bahia gold deposit, Carajás, Brazil. Mineral Deposita 30:30–38. https://doi.org/10.1007/BF00208874
6. Xie X, Byerly GR, Ferrell Jr. RE (1997) IIb trioctahedral chlorite from the Barberton greenstone belt: crystal structure and rock composition constraints with implications to geothermometry. Contrib Mineral Petrol 126:275–291. https://doi.org/10.1007/s004100050250